Redox-driven changes in organic C stabilization and Fe mineral transformations in temperate hydromorphic soils

Redox-driven changes in organic C stabilization and Fe mineral transformations in temperate hydromorphic soils

Beatrice Giannetta[a,b], Danilo Oliveira de Souza[c], Giuliana Aquilanti[c], Luisella Celi[a], Daniel Said-Pullicino[a]

[a]*Department of Agricultural, Forest and Food Sciences, University of Torino, Largo Paolo Braccini 2, 10095 Grugliasco, Italy*

[b]*Department of Biotechnology, University of Verona, Strada Le Grazie 15, 37134 Verona, Italy (Present address)*

[c]*ELETTRA Sincrotrone Trieste S.C.p.A., S.S. 14 Km 163.5, 34149 Basovizza, Trieste, Italy*

Corresponding author. E-mail address: beatrice.giannetta@univr.it

Abstract

Paddy soils experience long-term redox alternations affecting the interactions between the biogeochemical cycling of iron (Fe) and carbon (C). Differences in particle aggregation and soil organic matter (SOM) turnover are likely to both affect and be affected by the trajectory of Fe mineral evolution/crystallinity with redox fluctuations. We hypothesized that the legacy effects of redox cycling under paddy management affects particle aggregation, the distribution and mineralogy of Fe (hydr)oxides between particle-size fractions, and the interaction with SOM stabilization. Moreover, we expected underlying processes to be different in paddy eluvial and illuvial horizons, particularly due to the different inputs and redox conditions these horizons experience. To test these hypotheses, we evaluated the distribution of Fe species and organic C between different aggregate and particle-size fractions in topsoil (eluvial) and subsoil (illuvial) horizons of soils under long-term paddy and non-paddy management in NW Italy, as well as mineralogical changes in Fe phases by Fe K-edge Extended X-ray Adsorption Fine Structure (EXAFS) and X-ray Absorption Near Edge Structure (XANES) spectroscopy. Our findings indicate that although paddy topsoils are depleted in hydrous Fe oxides with respect to non-paddy soils, they can stabilize important amounts of C through mineral associations, particularly with finer particle-size fractions rich in less crystalline Fe phases. We also show that redox cycling can influence microaggregate stability and consequently the distribution of Fe phases and OC between intra and inter-microaggregate fractions. On the other hand, illuvial horizons under paddy management were enriched in short-range ordered hydrous Fe oxides and this contributed to enhanced microaggregate formation and C stabilization with respect to non-paddy subsoils.

Keywords: paddy soils, eluvial and illuvial horizons, physical fractionation, EXAFS, XANES, linear combination fitting.

1. INTRODUCTION

Paddy soils make up the largest anthropogenic wetlands on earth and store a large proportion of the global terrestrial carbon (C) stocks, representing a major terrestrial C pool, (ca.10 Pg) (Kirk, 2004). The greater soil organic C (SOC) accumulation rates in paddy topsoils with respect to non-paddy ones are generally assumed to be due to limited mineralization under anoxic soil conditions resulting from frequent field flooding (Cheng et al., 2009; Kalbitz et al., 2013; Kögel-Knabner et al., 2010; Pan et al., 2004). Although numerous studies attribute organic matter (OM) accumulation in paddy soils to this mechanism, there is growing evidence questioning this assumption (Huang and Hall, 2017).

Organic matter turnover and stabilization in paddy soils are strongly linked to the dynamic interactions with redox-active minerals, in particular iron (Fe) oxyhydroxides (Huang and Hall, 2017; Hall et al., 2018; Huang et al., 2020). Short-range-ordered (SRO) minerals (e.g., ferrihydrite) are able to stabilize more OC than well-ordered minerals (e.g., goethite, hematite and lepidocrocite) due to their larger surface area, and thus play a more important role in soil C storage mechanisms (Kramer and Chadwick, 2018; Lalonde et al., 2012; Torn et al., 1997). The role of SRO-Fe oxy-hydroxides in the preservation of SOC in paddy soils and OC persistence in deeper mineral horizons have been well-documented (Chorover et al., 2004; Huang and Hall, 2017; Kramer et al., 2012; Lalonde et al., 2012; Said-Pullicino et al., 2021; Wissing et al., 2014, 2013). However, further insights into the effects of redox alternations on Fe phase composition, crystal order and depth distribution, as well as the link between microaggregate formation and (de)stabilization, and OC stabilization mechanisms are necessary. Overall, depending on soil hydrology, paddy cultivation generally leads to a depletion in pedogenic Fe oxides in the topsoil due to their reductive dissolution and Fe leaching under reducing conditions, that is often accompanied by a relative increase in the proportion of SRO Fe oxides (Kölbl et al., 2014, Winkler et al., 2016). On the other hand, paddy subsoils are generally characterized by Fe oxide accumulation (Kölbl et al., 2014). In addition, redox fluctuations can potentially increase or decrease Fe crystallinity, depending on the environmental context (Coby et al., 2011; Ginn et al., 2017; Riedel et al., 2013; Thompson et al., 2006).

In upland soils SRO-Fe oxides can also promote aggregation (Oades and Waters, 1991, Xue et al., 2019), which indirectly enhances OM stability (Balesdent et al., 2000; Totsche et al., 2018). However, redox fluctuations are expected to influence aggregate

formation and stability with implications on the physical and chemical processes regulating OM stabilization. Selective microbial reduction and reprecipitation of Fe phases due to repeated redox cycles could therefore lead to a change in their distribution between different aggregate size classes. Recent studies have shown that a portion of Fe phases in soil can be protected from reductive dissolution (e.g., dithionite extraction) presumably due to their physical protection within microaggregates or co-precipitation with SRO aluminosilicates (Coward et al., 2018; Filimonova et al., 2016), suggesting the importance of aggregation/precipitation reactions. On the other hand, several studies showed that the reductive dissolution of Fe oxides involved in aggregate binding can disrupt aggregate stability (Huang et al., 2018; Henderson et al., 2012; De-Campos et al., 2009). Detailed chemical and size related characterization of soil aggregates and their depth distribution in rice paddies are scarce, even though such information is fundamental for further understanding the mechanisms controlling the biogeochemical cycling of elements in these agro-ecosystems.

The objectives of this work were to compare Fe mineral evolution and OC cycling in the topsoil and subsoil of a temperate paddy soil and an adjacent upland soil. We hypothesized that (1) in paddy topsoils, Fe redox cycling can lead to a depletion of pedogenetic Fe (hydr)oxides, promote microaggregate breakdown, and cause a redistribution of Fe phases with a relative increase in the proportion of SRO oxides and OC associated with the finest "free" particle-size fractions; and (2) the enhanced inputs of dissolved/colloidal Fe and OC entering the paddy subsoil through percolation can favour the accumulation of SRO Fe phases that contribute to the formation of stable microaggregates and C retention in illuvial horizons. To test these hypotheses, we evaluated the effects of redox cycling on the mineralogical changes and distribution/redistribution of Fe species (i.e., Fe in clays, SRO Fe(III) oxides such as ferrihydrite and organic Fe(III) complexes or more well-ordered Fe oxides), and OC between different intra- and inter-microaggregate particle-size fractions in topsoil (eluvial) and subsoil (illuvial) horizons of soils under long-term paddy (P) and non-paddy (NP) management in NW Italy. In order to study Fe transformations a combination of Fe K-edge Extended X-ray Adsorption Fine Structure (EXAFS) and X-ray Absorption Near Edge Structure (XANES) spectroscopy have been applied.

2. MATERIALS AND METHODS

2.1 Site description and sample collection

The study site is located in Zeme (Province of Pavia, NW Italy) (45°11'31.8″N; 8°40'3.7″E), in the plains of the River Po, between the Sesia and Agogna rivers and has a temperate climate, with a mean annual temperature of 12.5°C and mean annual precipitation of 950 mm. Soils develop on alluvial sediment with a maximum elevation of 80 m a.s.l., characterized by a high groundwater level during spring, up to 30-50 cm below surface. Two adjacent plots were identified for this study, one under maize (*Zea mays*) monocropping (NP, non-paddy) (45°11'33.6"N 8°40'06.1"E; 1.35 ha; Endogleyic Fluvisol) and another under paddy rice (*Oryza sativa*) monocropping (P, paddy management) established about 30 years ago (45°11'29.4"N 8°40'04.5"E; 4.43 ha; Haplic Gleysol). These non-calcareous soils generally had an acidic pH, low contents of OC and pedogenic Fe, and a sandy loam texture. A full description of the soil profiles and basic properties of the soil horizons under non-paddy and paddy management, as well as agricultural practices adopted are reported in Said-Pullicino et al. (2021). In March 2018, towards the end of the winter fallow period, topsoil and subsoil samples were collected from the Ap1, Ap2 and Bgw horizons in the non-paddy field and from the Arp1, Arp2, Arpd, Brd1 and Brd2 horizons in the paddy field from three replicated soil pits in each plot, and subsequently air dried and homogenized by passing through a 2-mm sieve. In this context, differences in analyzed soil properties under these contrasting cropping systems were attributed to the legacy of past management (non-paddy vs. paddy), and as such, were considered to be influenced by the long-term effects of different water management during the cropping season (irrigated vs. flooded) on soil redox conditions (rather than the specific redox conditions at the time of sampling). Moreover, this approach also integrated other effects, such as the slightly different quantity and quality of annual OM inputs with the incorporation of maize or rice crop residues, that were considered secondary and therefore not discussed in the present work.

2.2 Microaggregate separation and particle-size fractionation

The fractionation scheme adopted was intended to separate particle-size fractions distinguishing between those particles that constituted part of the stable microaggregates (intra-microaggregate particles size fractions) and particles of similar dimensions not involved in microaggregation (inter-microaggregate particle size fractions). This fractionation was carried out in three principal steps as illustrated in Figure S1:

(i) Soil microaggregates (53-200 μm) were first separated from all soil samples by means of a custom-built, mechanical wet sieving microaggregate isolator similar to

the Yoder sieve apparatus used for measuring aggregate stability, as follows. Aliquots of bulk soil (< 2 mm; 24 g) were transferred into 200 µm bucket sieves and immersed in large beakers filled with deionized water. Rotation of the buckets for 60 min in the presence of six metal beads was sufficient to break all macroaggregates. The coarse sand and particulate OM fraction (CSa+POM) remaining in the buckets was collected while the microaggregates and fine sand (53-200 µm) were separated from the suspension by passing through a 53 µm sieve.

(ii) The microaggregates and fine sand were resuspended in 200 ml water to which 15 drops of 1 M NaCl were added, rinsed until the supernatant had an EC ≤ 100 µS cm^{-1}, and subsequently sonicated with 400 J ml^{-1} to break microaggregates and ensure complete clay dispersion. Particle-size fractionation of the intra-microaggregate soil particles was carried out by sedimentation based on Stokes law to obtain coarse silt (20-53 µm; mCSi), fine silt (2-20 µm; mFSi) and clay (<2 µm; mCl) fractions within microaggregates. Finally, the fine sand fraction (FSa, 53-200 µm) was separated by passing through a 53 µm sieve.

(iii) The suspension remaining from (i) above, containing the inter-microaggregate and free soil particles (< 53 µm) was concentrated by repeated centrifugation (10,000 rpm) and supernatant siphoning, after addition of 2 ml of 1 M NaCl, taking care not to lose any fine mineral particles. The sediment was thereafter rinsed (until the supernatant had an EC ≤ 100 µS cm^{-1}), resuspended in 200 ml deionized water, and subsequently sonicated with 400 J ml^{-1} to ensure complete clay dispersion. Particle-size fractionation was carried out by sedimentation as described in (ii) above to obtain coarse silt (CSi), fine silt (FSi) and clay (Cl) fractions between microaggregates.

Each fraction was transferred into a pre-weighted container, freeze-dried, weighed and subsequently ground to < 0.5 mm for subsequent analysis.

2.3 OC and Fe contents characterization

Total OC content of the eight size fractions was determined by high temperature combustion using an elemental analyzer (NA 2100, Carlo Erba, Milan, Italy). Poorly crystalline Fe (Fe_o) was determined by extraction with 0.2 M ammonium oxalate at pH 3 as described by Schwertmann (1964), while more ordered Fe oxides (Fe_d) were determined by extraction with 0.3 M citrate-bicarbonate solution in the presence of sodium dithionite as described by Mehra and Jackson (1960). Metal concentrations in the

extracts were determined by atomic absorption spectroscopy (AAnalyst 400, Perkin Elmer). The ratio of the Fe_o/Fe_d, indicative of the contribution of the short-range ordered phases to total pedogenic oxides, or as the metric of Fe phase crystallinity, as well as their difference to estimate the content of more crystalline oxides (Fe_c), were calculated**.**

2.4 Fe K-edge XANES and EXAFS spectroscopy

X-ray absorption spectroscopic (XAS) analyses of FSa, CSi, mCSi, FSi, mFSi, Cl and mCl fractions were carried out at the XAFS beamline at Elettra Sincrotrone (Trieste, Italy) (Aquilanti et al., 2017; Di Cicco et al., 2009). The samples were prepared as pressed powders (*ca.* 15 mg) between Kapton® tape. Fe spectra were recorded in transmission mode using Si (111) monochromator, which was calibrated to the first-derivative maximum of the K-edge absorption spectrum of a metallic Fe foil (7112 eV). Spectra were acquired over an energy range between 6812-7660 eV with a variable step size (5 eV on the pre-edge region, 0.2 eV on the XANES region and a k constant step after XANES equal to 0.03 $Å^{-1}$) and integration time of 2 sec per point. The monochromator was detuned to exclude higher order harmonics. Two to six scans were collected and averaged to increase the signal-to-noise ratio. Prior to sample analysis, radiation damage was evaluated by recording a series of scans for a test sample over a duration similar to that required for actual spectra acquisition, and then comparing all XANES and EXAFS features of this sequence. We found that for the analytical conditions applied no photo-reduction due to the beam was observed. It is worth to note that a remarkable feature of XAFS beamline at Elettra is the unfocused beam, which makes the photon flux evenly spread over a large area of the sample minimizing (and in our case, preventing) any beam damage.

As previously described in Giannetta et al. (2020a, b), a suite of linear combination fitting (LCF) techniques designed to identify the major Fe components in the studied samples by comparison with the spectra of well characterized standards, was employed to analyze both the XANES and EXAFS data. Additional methods of analysis, such as Principal Component Analysis (PCA) (Table S1) and Target transformation, were used as a complementary tool during linear combination analysis.

XANES pre-edge peak analysis at the Fe K-edge was used to identify differences in the relative oxidation state between samples. Although redox conditions during sample collection and handling are known to affect Fe speciation (Prietzel et al., 2009), we attributed differences in Fe oxidation states to the legacy effects of long-term soil

management, rather than to the specific influence of reducing soil conditions during rice cropping. The energy position, intensity, and shape of the XANES are governed by the oxidation state and the specific bonding environment of the irradiated Fe atoms (coordination type, bonding symmetry, length to neighboring atoms (Westre et al., 1997; Wilke et al., 2001). Particularly, the pre-edge peak centroid energy position (PCE) allows a comparative evaluation of the oxidation state of Fe with values ranging between 7113.20 eV for Fe(II) and 7114.55 eV for Fe(III), and can be used for the quantification of Fe(II)/Fe(III) ratios of different Fe bearing minerals in soils with reasonable accuracy. According to Wilke et al. (2001) a linear relationship between the PCE and Fe(II)/Fe(III) ratio can be assumed, if the symmetry around Fe atoms remains the same for all samples. The pre-edge peak model and centroid determination was based on the considerations found on Wilke et al. (2001). Two pseudo-Voigt functions were considered as a component and their energy position, intensity and width were determined after the baseline extraction, which serves to remove the main absorption edge. Accordingly, it was assessed considering positions of individual components weighted by its respective intensity after the fit. A set of standard samples were also analyzed in the same way in order to get a reference value for Fe(II) and Fe(III) energy positions, respectively,7113.20 and 7114.55 eV. Siderite was used for Fe(II) whereas the average values of ferrihydrite, goethite, hematite were used as Fe(III) standards. The choice of these particular minerals was based on their probable presence in our samples according LCF results. The relative contribution of specific Fe compounds or compound classes to soils was also assessed by LCF performed on the entire XANES spectrum. Quantitative LCF was used for the speciation of different organic and inorganic Fe-bearing compounds. LCF on all normalized spectra was performed with the spectra of illite, smectite, nontronite, ferrihydrite, goethite, hematite, lepidocrocite, magnetite, maghemite, smectite, pyrite, purpurite, and Fe(III) citrate. The energy range for the fitting was 7105-7145 eV and the number of components to be include in a fit was determined after PCA on each group of samples (from the same horizon). Eventually, target transformations were used as a further parameter in the choice of the LCF result.

LCF analyses of k^3-weighted Fe and EXAFS spectra were performed over a k range of 2−10 $Å^{-1}$. EXAFS data processing (e.g., background removal, normalization and deglitching) and spectra generation were carried out with the software Athena. The qualitative speciation of Fe in the bulk soils and size-fractions by Fe K-edge EXAFS was carried out by comparison with several standards. Fe(III)-citrate is generally used as an

analog model compound for Fe(III)-OM complexes because it consists of Fe bound directly to OC (O'Day et al., 2004). We assumed that Fe EXAFS can be more suitable to quantify specific Fe oxyhydroxides (e.g. ferrihydrite, goethite, and hematite) and distinct Fe-organic compounds. Fe K-edge XANES can better estimate the relative contribution of different mineral classes and groups of organic compounds with different oxidation states of the Fe atom (e.g. Fe sulphides, Fe oxyhydroxides, Fe(II) and Fe(III)-organic complexes in mineral mixtures and soil samples.

The qualitative analysis of the nature of backscattering atoms in higher coordination shells was conducted using the Morlet wavelet transform (WT) method as implemented in the Igor Pro developed by (Funke et al., 2005). This method complements the conventional Fourier transform (FT) analysis and reveals the energies where back scattering takes place that give rise to the FT peaks. The WT modulus was analyzed and compared with the WT modulus for reference samples with contribution from C and/or Fe backscattering in the second coordination shell.

3. RESULTS

3.1 OC distribution in the different aggregate and particle-size fractions

Across all soil samples 40-60 % of total OC was associated with the finest particle-size fractions (<2 μm; Cl + mCl), while 20-40 % of total OC was associated with the coarser fractions and particulate OM (>53 μm; FSa + CSa+POM). Arp1 and Arp2 topsoil horizons of the P soil generally showed higher OC contents across most particle-size fractions with respect to the corresponding Ap1 and Ap2 horizons of the NP soil (Figure 1), in line with the higher total SOC contents of topsoils under paddy management. However, the most significant differences were observed for the 2-20 μm (FSi + mFSi) and >53 μm (FSa + CSa+POM) fractions in the more superficial horizon, that were on average 2.1 and 1.4-fold greater under P compared to NP management, respectively. OC associated with the finest particle fractions (Cl + mCl) that represented the greatest proportion of SOC, were only marginally though significantly higher in the P with respect to the NP soil in the first 15 cm of soil depth.

Paddy management also influenced the distribution of OC between intra- and inter-microaggregate particle-size fractions in the topsoil. Whereas P management resulted in a relatively higher intra:inter-microaggregate OC ratio for the fine silt-sized fraction (2-20 μm), lower ratios were generally observed for the clay-sized fraction with respect to NP soils (Figure 2a). In fact, on average 82 % of silt-associated OC in the P topsoils was

retained within microaggregates (c.f. 70 % in NP topsoils), while only 58 % of the total OC associated with clay-sized particles was intra-microaggregate OC with respect to 72 % in the NP soil.

Subsoil horizons under P management were particularly enriched in OC associated with the finest soil fractions (mCl + Cl; ~2.7-fold), with respect to the corresponding horizons in the NP soil (Figure 1). Moreover, in the paddy illuvial Brd1 horizon, up to 60 % of the clay-sized OC fraction was associated with stable microaggregates, compared to only 40 % in the Bgw horizon of the NP soil (mCl/Cl OC = 2.6 and 0.8, respectively). Although significantly less OC was associated with the silt-sized compared to the clay-sized particles in P subsoils (Figure 1), this former fraction showed the highest intra:inter-microaggregate OC ratio (Figure 2a).

3.2 Fe distribution in the different aggregate and particle-size fractions

Most of the pedogenic Fe in NP topsoils (53-58 %) was associated with the finest soil particles (<2 μm), primarily with intra-microaggregate clay particles (Figure 3a). Only around 25% of this Fe was oxalate-extractable as most Fe was in the form of more crystalline phases (Figures 3c and e). A substantial proportion of pedogenic Fe in these topsoils (around 28 %) was also associated with the coarser sand-sized fractions (CSa+POM and FSa) with an average Fe_o/Fe_d ratio of 0.5 (Table 1). In contrast, P topsoils were greatly depleted in pedogenic Fe showing around 70% less Fe associated with finer clay-sized and coarser sand-sized fractions with respect to the corresponding horizons in the NP soils, leading to a more even distribution of pedogenic Fe across particle-size fractions (Figure 3b). However, these observed differences in total pedogenic Fe contents did not seem to greatly influence the distribution of Fe between inter and intra-microaggregate Cl fractions, while a relative increase in intra-microaggregate Fe_d was observed for the FSi fraction (Figure 2b). On the other hand, the distribution between more and less crystalline phases was influenced by management as clay and sand-sized fractions showed a greater proportion of oxalate-extractable Fe and higher Fe_o/Fe_d ratios (up to 0.8) with respect to NP topsoils (Table 1).

Subsoil horizons in P and NP profiles showed evident management-related differences in the distribution of pedogenic Fe between aggregate and particle-size fractions. Whereas, NP subsoil samples from the Bgw horizon showed lower total pedogenic Fe contents with respect to the overlying Ap soil horizons (Fig. 3a) albeit very similar intra:inter-microaggregate Fe_d (Figure 2b) and Fe_o/Fe_d ratios (Table 1) across fractions, P subsoils

showed higher total pedogenic Fe contents and oxalate-extractable Fe with respect to both P topsoils (Arp1 and Arp2 horizons) and the corresponding subsoil horizon in the NP soil (Bgw). The most enriched Brd1 illuvial horizon in the P soil had pedogenic Fe contents associated with the fine silt and clay-sized fractions that were respectively 3 and 6-fold higher compared to the corresponding subsoil Bwg horizon in the NP soil. The substantial enrichment in pedogenic Fe associated with the finest soil fraction (< 2 μm) of the Brd1 horizon was mainly due to an increase in Fe_c (Figure 3d) that was also responsible for the lower Fe_o/Fe_d ratio observed with respect to the topsoils (Table 1). Although only limited changes in the distribution of pedogenic Fe between intra and inter-microaggregate fractions across different particles sizes was observed with soil depth in the P soil, the fine silt and clay-sized fractions of the Brd1 showed slightly higher intra:inter-microaggregate Fe_d ratios with respect to the corresponding subsoil horizon in the NP soil (Figure 2b).

3.3 Fe speciation in the different aggregate and particle-size fractions

NP soils showed minor variations in centroid position values with soil depth although clear differences were observed between particle-size fractions (Figure 4). PCE values tended to increase with decreasing particle size with a maximum difference of around 0.7 eV between FSa and Cl fractions, albeit no differences between intra- and inter-microaggregate fractions were observed (Figures 4 and S2; Table S2). Mean PCE values for the clay-sized fractions around 7114.59 eV suggest that Fe-containing mineral phases in this fraction were mostly oxidized. On the other hand, an increasing contribution of Fe(II) was observed for the FSa and CSi fractions with PCE values around 7113.93 eV.

Similar differences in PCE values between particle-size fractions were also observed in the P soils, although in contrast to NP soils, clear trends with soil depth were noted (Figure 4). Across all particle-size fractions, lower PCE values were generally obtained for topsoils with respect to subsoil horizons suggesting a greater contribution of Fe(II) to total Fe in the superficial horizons. The difference in PCE values between topsoils and subsoils was generally less pronounced for the finest clay-sized fractions (0.15 eV) with respect to the other fractions (0.18-0.34 eV), suggesting a greater contribution of reduced Fe in the coarse-sized fractions separated from P topsoils.

The deconvolution of the XANES spectra in the energy range between 7105 eV and 7145 eV of both NP and P soils by LCF (Table 2) showed that Fe phases were adequately described by three or four components. The major differences in the relative contribution

of different Fe phases were linked to the different particle-size fractions rather than soil management and depth. According to the LCF results (Table 2), in the NP soil the FSa fractions contained relatively high proportions of chlorite (32-34%) that tended to decrease with decreasing particle-size, and siderite (26-33%) that was absent in the other fractions. Other minor phases in this fraction included illite (13-21%) and hematite (20-22%). Similarly, Fe phases in the coarse silt-sized fractions (CSi and mCSi) were also represented by chlorite (22-27%), illite (34-66%) and hematite (13-27%). Minor proportions of magnetite were also detected in this fraction (5-14%). Fine silt-sized fractions (FSi and mFSi) generally showed smaller proportions of chlorite (12-27%) and illite, though other Fe-containing minerals like smectite and nontronite were detected, as well as minor contributions (<10%) from organically complexed Fe(III). In contrast to the other fractions, the finest clay-sized fractions (Cl and mCl) were characterized by the absence of illite and the presence of relatively high amounts of nontronite that represented up to 79-83% of the Fe phases. This particle-size fraction also contained variable contributions from Fe oxide phases (e.g., lepidocrocite and ferrihydrite) as well as organically complexed Fe(III). Overall, in NP, the major differences in the relative contribution of different Fe phases were linked to the different particle-size fractions rather than depth.

In the P soils, the FSa fraction contained similar contents of chlorite (32-34%), and siderite (27-32%) as observed for the same fraction in NP. Other minor phases in this fraction included illite and hematite. Fe phases in the coarse silt-sized fractions were also represented by chlorite (18-27%), illite (39-75%) and hematite (9-23%) though with slightly different relative contributions. As for NP soils, fine silt-sized fractions (FSi and mFSi) generally contained chlorite (23-29%) and illite, smectite (16-57%) and nontronite (7-32%), as well as minor contributions (<10%) from organically complexed Fe(III). The clay-sized fractions were characterized by the absence of illite and the presence of relatively high amounts of nontronite that represented up to 79-84% of the Fe phases. This particle-size fraction also contained variable contributions from Fe oxide phases (e.g. lepidocrocite and ferrihydrite) as well as organically complexed Fe(III). These were most abundant in P subsoils.

3.4 Fe EXAFS linear combination fitting and WT results

EXAFS spectra of all size-fractions were accurately reconstructed by three or four components, and quantitative results of the LCF evidenced that Fe phases in all NP and

P soils were mainly characterized by the presence of chlorite, ferrihydrite, lepidocrocite, and Fe(III)-citrate (Figure 5, Tables 3 and S3).

LCF results for the size fractions, with the only exception of FSa, using three components are reported in Figure 6 and the sample fit (dotted lines) is labeled with the R-factor. Fe K-edge EXAFS spectra showed features at ~4.0 $Å^{-1}$ (maximum 1), ~6.5 $Å^{-1}$ (maximum 2), ~7.5 $Å^{-1}$ (maximum 3), ~8.5 $Å^{-1}$ (maximum 4). The maximum at 4.0 $Å^{-1}$ has different features in ferrihydrite and lepidocrocite (insert in Figure 5). The maximum at 7.5 $Å^{-1}$ is characteristic of ferrihydrite, whereas the small maximum at 8 $Å^{-1}$ is typical of lepidocrocite and magnetite, and a broad one describes Fe(III)-citrate spectrum. The maximum at 8.5 $Å^{-1}$ is also a characteristic feature of ferrihydrite. The maximum at 10 $Å^{-1}$ is only characteristic of lepidocrocite (insert in Figure 5). The maxima at 6.5 and 7.5 $Å^{-1}$ (as also at 8.5 $Å^{-1}$) are characteristic of ferrihydrite (Figure 5).

Quantitatively, NP soils evidenced an increase in the relative abundance of ferrihydrite and Fe(III)-citrate phases with decreasing particle size, together constituting around 20-24 % and 9-21%, respectively in the coarse silt (CSi, mCSi) and both 31-43% in the clay-sized (Cl, mCl) fractions, with no evident trends with soil depth (Table 3). On the other hand, the relative abundance of chlorite was lower in the clay-sized fractions (4-15 %) with respect to the other fractions (30-49%), while lepidocrocite accounted for around 11-19% of Fe phases across size fractions. Only the coarser FSa fraction was characterized by the presence of more crystalline Fe phases like hematite and goethite. Similarly, P soils showed and increasing abundance of ferrihydrite and Fe(III)-citrate phases with decreasing particle size, from 8-31 % and 9-29 % in the coarse-silt fractions (CSi, mCSi) to 9-41 % and 22-46 % in the clay-sized (Cl, mCl) fractions, respectively. Chlorite ranged from 9 to 66 % and lepidocrocite from 11 to 19 % across size fractions. However, in contrast to NP soils, P soils evidenced lower contents of ferrihydrite in the topsoils and more pronounced variations in the relative abundance of ferrihydrite, more crystalline Fe phases and Fe(III)-citrate with soil depth (Table 3). Considering exclusively the finest clay-sized fraction, the relative content of ferrihydrite increased from around 14-20 % in the Arp1 and Arp2 horizons to 40% in the Brd1 horizon, while Fe(III)-citrate decreased from 41-46 % in the topsoils to 30% in the subsoils. Magnetite (up to 15 %) was also detected associated with the clay-sized fractions in the Brd2 horizon.

A key in the study of Fe associated with OM by EXAFS is a proper analysis of the second coordination shell. In traditional analysis of EXAFS spectra it is difficult to separate the contributions from different backscattering atoms in higher coordination

shells present at similar bonding distances from the central Fe atom. Complementary to LCF, WT provides useful information simultaneously resolving data in both wave space (k) and interatomic distance (R) space, and the resulting k−R maps are helpful for improving the fitting model and understanding elemental speciation in the sample. In addition, WT analysis was used to qualitatively test the presence of Fe back-scatterers in the second coordination shell of Fe. The Morlet wavelet transforms of k^3-weighted Fe K-edge EXAFS spectra of the samples over a R + ΔR-range of 2.2-4.0 Å was calculated and the resulting wavelet plots compared with those of Fe(III) reference compounds (ferrihydrite, Fe(III)-citrate, chlorite). Figure S3 shows the WT plots of the standards. In the ferrihydrite plot, the Fe shell contributes a strong feature at 7-8 $Å^{-1}$ and 2.75 Å (Daugherty et al., 2017). In the Fe(III)-citrate standard, the absence of Fe backscattering is accompanied by new features at distances of 2.0–2.5 Å and indicates back-scattering from lighter atoms, in agreement with single and multiple backscattering from C/O in the second and third coordination shells of tris(oxalato)Fe(III) (Daugherty et al., 2017; Karlsson and Persson, 2010). Moreover, these features appear at lower energies (3–4 $Å^{-1}$) than those of Fe.

The WT of the EXAFS data (η=8, σ=1) of the CSi, FSi, Cl and relative aggregated fractions showed that both the intensity caused by light back-scatterers at low k-values and by heavier atoms at higher k varied among the samples (Figure 6), compared to the WT plots of standards (Figure S3). A general trend was observed with decreasing particle-size from the CSi to the Cl fraction in the NP topsoil horizons (Ap1 and Ap2; Figure 6a). The clay samples generally have more intense maxima near 8 A^{-1}, typical of ferrihydrite. A slight increase in the Fe-SOM signal contribution at above 2.2 Å and 2–4 $Å^{-1}$ is also present, as reported in the EXAFS LCF results, while the CSi fractions clearly match with the high chlorite content. In the Bgw fraction the increasing content of ferrihydrite (up to 50% considering 3 components) is evident in the intense peak at 8 A^{-1} in the Cl and mCl. Although an increase in Fe oxides and organically-complexed forms occurred from the coarse to the fine fractions, significant differences were not found ranging from the topsoil to the subsoil in NP soil.

Considering the equivalent topsoil horizons under P management, spectra of the Arp1 and Arp2 horizons are characterized by features indicating an increase in Fe-SOM and ferrihydrite with decreasing particle-size from the CSi to the Cl fraction (Figure 6b). In addition, the mCl fraction, as also reported in the LCF performed using three components, clearly matches lepidocrocite features. In the Arpd horizon of the P soil the increasing

contribution of ferrihydrite (from 21 to up to 28% from the CSi to the Cl fraction) and Fe-SOM (from ca. 18 to ca. 38% from the CSi to the Cl fraction) are also reported in the WT of the EXAFS data. In the Brd1 horizon the higher Fe(III)-SOM content in the Cl with respect to the mCl fraction is evident. As also evidenced by the LCF, CSi contains less ferrihydrite than mCSi. Compared to the Brd1 horizon, in the Brd2 horizon the ferrihydrite content decreased, whereas the increased Fe(IIII)-SOM contents, in all the fractions, appear as a clear feature.

4. DISCUSSION

4.1 Influence of paddy management on OC distribution in the aggregate and particle-size fractions in topsoils and subsoils

The larger accumulation of OM in soils under paddy management with respect to other arable ecosystems has been widely recognized to contribute to the C sink functions of rice agro-ecosystems (Kalbitz et al., 2013; Kögel-Knabner et al., 2010; Wissing et al., 2011). This has often been attributed to the retarded decomposition of OC under waterlogged conditions during several months of paddy field flooding every year (Sahrawat, 2004), although enhanced soil microaggregation (Wissing et al., 2014) and specific organo-mineral associations have also been shown to drive OC accrual in these soils (Winkler et al., 2019). Apart from confirming the greater OC contents in P with respect to NP topsoils, this study also suggests that retarded decomposition could be partly responsible for the higher contents of particulate OM associated with the coarser size fractions under paddy management. This is in line with the findings of Chen et al. (2021) who showed that SOC sequestration in paddy soils is partly linked to the accumulation of crop residue-derived labile C. Although paddy management resulted in a greater amount of particulate OM responsible for around 25 % of total SOC, mineral-associated OM still represented the greatest proportion of SOC. The interaction of OC with soil minerals and its subsequent stabilization against microbial mineralization largely depend on soil redox conditions (Eusterhues et al., 2014). In fact, long-term paddy management favored OC stabilization through this mechanism as P soils showed higher amounts of OC associated with the finer soil fractions with respect to NP soils, not only in the topsoil but also in the subsoil. Moreover, our results evidenced that whereas the clay-sized fraction is the main OC sink in both paddy topsoil and illuvial horizons (40 and 47-62 %, respectively), OC associated with the fine silt-sized fraction can also represent a substantial proportion of total SOC in P topsoils (on average 23 % of total SOC). This was assumed to be linked to the presence

of a substantial proportion of pedogenetic Fe oxides (26 %) in this fraction probably due to their redistribution from the finer to coarser fractions with repeated cycles of Fe(III) reduction and re-oxidation/precipitation that characterize these topsoils.

OC stabilization in the paddy soils was not only affected by particle size but also related to redox-driven changes in microaggregate formation and stability. Paddy management resulted in relatively lower contents of OC associated with the intra-microaggregate clay-sized particles in the topsoil with respect to the NP soil, but favored the presence of OC associated with the intra-microaggregate fine silt-sized particles. Aggregate stability may be somewhat compromised in soils subjected to alternating redox conditions possibly due to the disruptive energy occurring upon slaking (Six et al., 2000), and reductive dissolution of Fe oxides that are known to serve as binding agents holding aluminosilicate particles together (Blankinship et al., 2017; De-Campos et al., 2009). Our results suggest that clay-sized particles are more prone to dispersion during microaggregate breakdown under alternating redox conditions probably due to their more negative surface charge and greater susceptibility of the SRO-Fe oxides holding aluminosilicate particles together to microbial reduction. In contrast, the higher amount of OC associated with silt-sized particles within microaggregates under paddy management suggests that this size fraction could be less susceptible to aggregate breakdown under anoxic conditions and therefore represent an important pool of stable OC in these soils. This is also corroborated by the higher ratio of intra:inter-microaggregate pedogenic Fe and lower Fe_o/Fe_d ratio observed for the silt-sized with respect to the clay-sized fractions in the P topsoils. Our findings therefore partially confirm our first hypothesis that paddy management may affect the distribution of OC between different particle-size fractions due to the influence of redox cycling on aggregate stability. Huang et al. (2018) previously reported how management-induced soil aggregate turnover and OC stabilization was strongly linked to Fe cycling in a rice-wheat crop rotation, particularly when exogenous OM was applied. Similarly, De-Campos et al. (2009) showed that the reductive dissolution of poorly ordered Fe oxides involved in aggregate binding may lead to changes in the morphology of soil particles, favour colloid dispersion and contribute to a decrease in aggregate stability under anoxic conditions. However, notwithstanding the depletion of total pedogenetic Fe in the topsoil (about 50% less Fe_d), more OC is stabilized by association with the finest soil particles both within and outside microaggregates (about 25% more OC) with respect to non-paddy soils. In paddy topsoils coprecipitation, known to retain more OC with respect to surface

adsorption on Fe (hydr)oxides and leading to the formation of Fe-OM associations with a high C/Fe ratio (Sodano et al., 2017), may in fact represent an important mechanism for protected OM from microbial degradation (Ginn et al., 2017) and thus contribute to OC accumulation. This was also confirmed by EXAFS LCF that evidenced a substantial proportion of Fe-OM phases (up to 45%) and ferrihydrite (up to 20%) in the clay-sized fractions (Table 3).

The significant enrichment in OC associated with intra-microaggregate clay-sized particles in the P subsoil horizons when compared to the corresponding horizons in the NP soil suggest that microaggregate formation and stabilization in the subsoil may also contribute to the preservation of OC and could be linked to the mobilization of dissolved OC and Fe from the topsoil during the rice cropping season when the paddy fields are flooded (Said-Pullicino et al., 2016), confirming our second hypothesis. In a previous study (Said-Pullicino et al., 2021) we provided evidence that colloid transport, together with the percolation of Fe^{2+} and subsequent precipitation of SRO oxides in the oxic subsoil horizons, could contribute to the accumulation of Fe and OC in the illuvial horizons. In the present study, we are further showing that these redox-driven dynamics may also contribute to microaggregate formation and soil OC stabilization in the deeper soil horizons of temperate paddy soils.

4.2 Fe mineral transformations and distribution in the different aggregate and particle-size fractions

As expected, paddy management resulted in a general depletion in both SRO and crystalline Fe oxides in the topsoil with respect to the non-paddy soil, probably due to the reductive dissolution of Fe oxides and subsequent leaching into the subsoil with repeated redox cycles, as suggested by Said-Pullicino et al. (2021). Nonetheless, the higher Fe_o/Fe_d ratio of the clay-sized fractions (Table 1) indicate a relative increase in SRO Fe oxides associated with this fraction primarily in the form of ferrihydrite and Fe-OM complexes (Table 3). In redox-active paddy topsoils, repeated reductive dissolution of both crystalline and less ordered Fe oxides under anoxic conditions with subsequent release of high concentrations of dissolved Fe^{2+} and DOC (Bertora et al., 2018; Said-Pullicino et al., 2016), followed by the oxidative re-precipitation with the re-establishment of oxic conditions or in the O_2-rich rice rhizosphere, can lead to the formation of new mineral phases, mainly SRO oxides more or less associated with phyllosilicate particles (Sodano et al., 2016) or Fe-OC coprecipitates (Sodano et al., 2017). The presence of minor

amounts of lepidocrocite (around 12-15 %) also suggests that the Fe^{2+}-catalyzed recrystallization or solid state transformations of ferrihydrite to more thermodynamically stable phases can also occur to some extent. Chen and Thompson (2021) report that the nature of the new Fe minerals formed as a result of Fe(II) oxidation may be directed by the relative presence of OM and Fe phases in the soil, that can either hinder or promote crystal growth and the formation of more crystalline phases, respectively. It is thus highly likely that in the studied soils that are relatively poor in pedogenic Fe but that hold important amounts of OM (Said-Pullicino et al., 2021), the trajectory of Fe minerals under paddy management tends towards the relative accumulation of SRO Fe(III) phases. Our results further show that redox-driven Fe phase transformations may also involve changes in microaggregate stability that consequently influences the association of new mineral phases with more aggregated (for fine silt-sized) or dispersed (for clay-sized) mineral particles (Figure 2b). EXAFS LCF suggests that hydrous Fe minerals present in the clay and silt-sized fraction of paddy topsoils are mainly represented by ferrihydrite (about 18 and 14 %, respectively) and Fe-OM phases (about 45 and 30 %, respectively) confirming the role these size-fractions may play in OC retention.

The lower PCE values generally observed across particle-size fractions in paddy topsoils with respect to both paddy subsoils and non-paddy topsoils (Figure 4) suggest that in this redox-active horizon a proportion of Fe in the mineral phase may remain in its reduced form even after field drainage. XANES LCF suggests that this may be due to the reduction of structural Fe present in phyllosilicate structures (nontronite and smectite in the finer fractions, and chlorite in the coarser fractions) under anaerobic conditions (Table 2). Various studies have shown that the biological reduction of Fe(III) in phyllosilicates like nontronite (Zhao et al., 2013) and illite-smectite mixed layers (Shelobolina et al., 2012) is possible in soils subject to reducing conditions (Liao et al., 2019; Neumann et al., 2015; Ribeiro et al., 2009; Dong et al., 2009 and references therein) to an extent that depends on the location of Fe(III) within the clay structure (Shi et al. 2021). However, the similar proportions of nontronite in P and NP topsoils suggest that this redox-cycling under paddy management did not lead to *in situ* loss of structural Fe. Similar results were obtained by Vogelsang et al. (2016) after one year of incubation of nontronite in a paddy soil. Akter et al. (2018) have also shown that reduction of octahedral Fe^{3+} in clay minerals and their interstratified forms could be responsible for accepting electrons during OM mineralization under anaerobic conditions. Vertical redox gradients and OM contents in hydromorphic soils can therefore exert a major control on the oxidation state of structural

Fe in phyllosilicates and other Fe containing minerals (Chen et al. 2017). However, with the re-establishment of oxic conditions, structural Fe in clay minerals can be rapidly reoxidized (within days) to Fe(III) through abiotic or biotic oxidation, as reported for chlorite and nontronite-associated Fe(II) by Zhang et al. (2011) and Shi et al. (2021). It is however possible that in under oxic conditions reduced Fe was preferentially reoxidized in smaller particles having higher contact surfaces with O_2 while reoxidation was slower in larger size fractions and within microaggregates. This would partially explain the increasing presence of reduced Fe(II) with increasing particle size in the redox-dynamic topsoils, even if the soils were already oxic during sampling. The lower PCE values in the coarser soil fractions may also be due to the precipitation of Fe(II) carbonates. XANES LCF evidenced that the precipitation of siderite is evidently not associated with the fine particle-sizes like most other secondary minerals, but eventually other mechanisms (e.g., linked with high rates of CO_2 production during the mineralization of particulate OM) may drive their precipitation on coarser fractions (Table 2). However, due to the presence of similar proportions of siderite in the coarse fractions of both paddy and non-paddy topsoils and subsoils we cannot exclude a lithogenic origin of this mineral. Siderite oxidation kinetics are known to be relatively slow as structurally bound Fe(II) in carbonates are not particularly electro-active due to the low Fe(II) surface density, and rates of oxidation are generally slower with increasing nominal particle size (Hoving et al. 2017) or due to surface passivation of the mineral by organic ligands (Rothwell and Kretzschmar, 2020). Nonetheless, the different trend in PCE values for this fraction in paddy and non-paddy soils suggests that redox-cycling in the former can affect the oxidation state of Fe phases along the soil profile and that Fe K-edge XANES can adequately evaluate these changes.

Our results also evidenced that paddy illuvial horizons just beneath the plough pan can accumulate remarkable amounts of Fe (hydr)oxides particularly associated with the finest particle fractions and also contribute to microaggregate formation and stabilization (Figure 3). This is consistent with the inputs of colloidal and/or dissolved Fe from the topsoil and the larger Fe oxide stocks in the subsoil (about 40 % higher) with respect to adjacent non-paddy soils reported for temperate paddy soils by Said-Pullicino et al. (2021). EXAFS LCF suggested that most of the Fe phases associated with the finest particle fractions in the Brd1 horizon were represented by ferrihydrite (40%) and Fe-OM forms (30%) confirming that these subsoil horizons can play an important role in OC accumulation in rice paddy soils. However, we did not observe substantial differences in

622 the mineral composition of pedogenetic Fe phases in paddy and non-paddy subsoils
623 (Table 3). Nor was the transformation of ferrihydrite into more crystalline phases
624 particularly expressed because interaction with dissolved OM could have inhibited the
625 Fe^{2+}-catalyzed transformation into more crystalline phases even in the subsoil.
626 Nonetheless, the increasing trend in PCE with soil depth under paddy but not under non-
627 paddy management (Figure 4) clearly suggests that redox cycling in paddy topsoils
628 contribute reduced Fe forms, while Fe phases in the subsoil are mostly oxidized, except
629 for the coarser-size fractions where siderite was detected (Table 2). In these paddy fields,
630 subsoil horizons just beneath the plough pan generally remain prevalently oxic even when
631 the topsoils are flooded, as the rising ground water table during spring and summer (up
632 to around 40 cm below the soil surface) does not limit oxygen diffusion until late in the
633 cropping season (mid-July). **4.3 Potential and limitation of Fe K-edge XANES and**
634 **EXAFS for Fe speciation in soil fractions**
635 This work together with the results of previous studies carried out on well-defined binary
636 and ternary mixtures of different Fe-bearing minerals (e.g., Wilke et al., 2001; O'Day et
637 al., 2004; Prietzel et al., 2007) showed that Fe K-edge XANES can provide an estimate
638 of the relative contribution of different mineral classes and groups of organic compounds
639 with different oxidation state of the Fe atom (e.g., Fe(II) sulphides versus Fe(III)
640 oxyhydroxides; Fe(II)-organic complexes versus Fe(III)-organic complexes) by
641 calculating the PCE and applying LCF to the entire XANES spectrum. In soils this
642 evaluation is complicated by the presence of mixed Fe phases that form during
643 pedogenesis. Therefore, accurate quantification of different Fe phases in soils by Fe K-
644 edge XANES will probably always remain difficult to achieve particularly in
645 environments experiencing dynamic redox conditions. At present, LCF conducted on the
646 XANES spectrum in an energy range between 7105 and 7145 eV allows the quantification
647 of specific minerals in soils approximately, but not accurately. The accuracy of the results
648 of the LCF procedure is strongly affected by the correctness of the applied set of predictor
649 variables. LCF on the XANES spectrum revealed a systematic influence of increasing
650 oxidizing conditions on the Fe speciation in the topsoil and the subsoil of paddy soil: the
651 contribution of Fe(III) compounds increased with soil depth and decreasing particle size
652 fractions, especially in the aggregated ones. This study highlights the potential of Fe K-
653 edge XANES for the determination of Fe speciation in redoximorphic soils and soil
654 fractions, despite its present problems and limitations. With Fe K-edge XANES, the
655 proportion of Fe(II) and Fe(III) and the relative contribution of different Fe compounds

in soil samples and soil aggregates can be evalutaed. However, although Fe K-edge XANES can estimate fairly well the relative contribution of different mineral classes and groups of organic compounds with different oxidation states of the Fe atom in mineral mixtures and soil samples, it fails to quantify specific Fe oxyhydroxides (e.g., ferrihydrite, goethite, and hematite) or distinct Fe-organic compounds. Thus, a combination with Fe EXAFS, as also WT, allows the speciation of Fe in different fractions and aggregates in soils subjected to dynamic redox conditions.

5. CONCLUSIONS

Evaluating the mechanisms for OC stabilization in paddy soils still deserves attention particularly due to the complex interactions between C cycling and changes in the contents and mineralogy of hydrous Fe oxides in redox-active systems. In this study, we linked the enhanced stabilization of OC in temperate paddy soils to the redox-driven changes in Fe phases (evaluated by Fe K-edge XANES and EXAFS spectroscopy) and their distribution between aggregate and particle-size fractions. Our findings have shown that although paddy topsoils show higher contents of particulate OC in the coarser size-fractions with respect to non-paddy soils, most of the SOC is associated with the finer soil fractions, not only in the topsoil but also in the subsoil. This suggests that the management-induced differences in C stocks is not primarily due to the limited decomposition of crop residues under paddy management, but rather to the redox-driven changes in the association of OC with soil minerals. We show that OC stabilization through interaction with minerals is also affected by microaggregate stability. Paddy management may lead to microaggregate breakdown with a preferential release of clay-sized particles rich in both SRO Fe oxides and OC, while intra-microaggregate fine silt-sized particles may also serve as an important OC sink. Long-term alternating redox conditions generally resulted in paddy topsoil horizons that were depleted in pedogenic Fe with respect to non-paddy soils, and led to a redistribution of Fe phases across different particle size fraction often as less crystalline phases (primarily ferrihydrite and Fe-OM associations). Nonetheless, the higher C contents indicate that higher C loadings can be achieved under these redox-dynamic environments. Moreover, illuvial horizons under paddy management were enriched in SRO hydrous Fe oxides and this contributed to enhanced microaggregate formation and C stabilization with respect to non-paddy subsoils.

Acknowledgements

This study was partly funded by the University of Torino as part of the research project "Colloid mobility and organic matter stabilization in hydromorphic soils". We also like to express our gratitude to Marco Romani for his assistance with sample collection.

References

Akter, M., Deroo, H., De Grave, E., Van Alboom, T., Kader, M.A., Pierreux, S., Begum, M.A., Boeckx, P., Sleutel, S., 2018. Link between paddy soil mineral nitrogen release and iron and manganese reduction examined in a rice pot growth experiment. Geoderma 326, 9–21. https://doi.org/10.1016/j.geoderma.2018.04.002

Aquilanti, G., Giorgetti, M., Dominko, R., Stievano, L., Arčon, I., Novello, N., Olivi, L., 2017. *Operando* characterization of batteries using x-ray absorption spectroscopy: advances at the beamline XAFS at synchrotron Elettra. J. Phys. D. Appl. Phys. 50, 074001. https://doi.org/10.1088/1361-6463/aa519a

Balesdent, J., Chenu, C., Balabane, M., 2000. Relationship of soil organic matter dynamics to physical protection and tillage. Soil Tillage Res. 53, 215–230. https://doi.org/10.1016/S0167-1987(99)00107-5

Bertora, C., Cucu, M.A., Lerda, C., Peyron, M., Bardi, L., Gorra, R., Sacco, D., Celi, L., Said-Pullicino, D., 2018. Dissolved organic carbon cycling, methane emissions and related microbial populations in temperate rice paddies with contrasting straw and water management. Agric. Ecosyst. Environ. 265, 292–306.

Blankinship, J.C., Fonte, S.J., Six J, Schimel, J.P., 2016. Plant versus microbial controls on soil aggregate stability in a seasonally dry ecosystem. Geoderma 272, 39–50. https://doi.org/10.1016/j.geoderma.2016.03.008

Chen, X., Hu, Y., Xia, Y., Zheng, S., Ma, C., Rui, Y., He, H., Huang, D., Zhang, Z., Ge, T., Wu, J., Guggenberger, G., Kuzyakov, Y., Su, Y., 2021. Contrasting pathways of carbon sequestration in paddy and upland soils. Glob. Chang. Biol. 27, 2478–2490. https://doi.org/10.1111/gcb.15595

Chen, C., Kukkadapu, R.K., Lazareva, O., Sparks, D.L., 2017. Solid-phase Fe speciation along the vertical redox gradients in floodplains using XAS and Mössbauer spectroscopies. Environ. Sci. Technol. 2017, 51, 7903−7912. https://doi.org/10.1021/acs.est.7b00700

Chen, C., Thompson, A., 2021. The influence of native soil organic matter and minerals on ferrous iron oxidation. Geochim. Cosmochim. Acta 292, 254–270. https://doi.org/10.1016/j.gca.2020.10.002

Cheng, Y.Q., Yang, L.Z., Cao, Z.H., Ci, E., Yin, S., 2009. Chronosequential changes of selected pedogenic properties in paddy soils as compared with non-paddy soils. Geoderma 151, 31–41. https://doi.org/10.1016/j.geoderma.2009.03.016

Chorover, J., Amistadi, M.K., Chadwick, O.A., 2004. Surface charge evolution of mineral-organic complexes during pedogenesis in Hawaiian basalt. Geochim. Cosmochim. Acta 68, 4859–4876. https://doi.org/10.1016/j.gca.2004.06.005

Coby, A.J., Picardal, F., Shelobolina, E., Xu, H., Roden, E.E., 2011. Repeated anaerobic microbial redox cycling of iron. Appl. Environ. Microbiol. 77, 6036–6042. https://doi.org/10.1128/AEM.00276-11

Coward, E.K., Thompson, A., Plante, A.F., 2018. Contrasting Fe speciation in two humid forest soils: insight into organomineral associations in redox-active environments. Geochim. Cosmochim. Acta 238, 68–84. https://doi.org/10.1016/j.gca.2018.07.007

Daugherty, E.E., Gilbert, B., Nico, P.S., Borch, T., 2017. Complexation and redox buffering of iron(II) by dissolved organic matter. Environ. Sci. Technol. 51, 11096–11104. https://doi.org/10.1021/acs.est.7b03152

De-Campos, A.B., Mamedov, A.I., Huang, C.-H., 2009. Short-term reducing conditions decrease soil aggregation. Soil Sci. Soc. Am. J. 73, 550-559. https://doi.org/10.2136/sssaj2007.0425

Di Cicco, A., Aquilanti, G., Minicucci, M., Principi, E., Novello, N., Cognigni, A., Olivi, L., 2009. Novel XAFS capabilities at ELETTRA synchrotron light source. J. Phys. Conf. Ser. 190. https://doi.org/10.1088/1742-6596/190/1/012043

Dong, H.L., Jaisi, D.P., Kim, J., Zhang, G.X., 2009. Microbe-clay mineral interactions. Am. Mineral. 94, 1505–1519. https://doi.org/ 10.2138/am.2009.3246

Eusterhues, K., Hädrich, A., Neidhardt, J., Küsel, K., Keller, T.F., Jandt, K.D., Totsche, K.U., 2014. Reduction of ferrihydrite with adsorbed and coprecipitated organic matter: Microbial reduction by Geobacter bremensis vs. abiotic reduction by Na-dithionite. Biogeosciences 11, 4953–4966. https://doi.org/10.5194/bg-11-4953-2014

Filimonova, S., Kaufhold, S., Wagner, F.E., Häusler, W., Kögel-Knabner, I., 2016. The role of allophane nano-structure and Fe oxide speciation for hosting soil organic matter in an allophanic Andosol. Geochim. Cosmochim. Acta 180, 284–302. https://doi.org/10.1016/j.gca.2016.02.033

Funke, H., Scheinost, A.C., Chukalina, M., 2005. Wavelet analysis of extended x-ray absorption fine structure data. Phys. Rev. B 71, 094110. https://doi.org/10.1103/PhysRevB.71.094110

Giannetta, B., Plaza, C., Siebecker, M.G., Aquilanti, G., Vischetti, C., Plaisier, J.R., Juanco, M., Sparks, D.L., Zaccone, C., 2020a. Iron speciation in organic matter fractions isolated from soils amended with biochar and organic fertilizers. Environ. Sci. Technol. 54, 5093–5101. https://doi.org/10.1021/acs.est.0c00042

Giannetta, B., Siebecker, M.G., Zaccone, C., Plaza, C., Rovira, P., Vischetti, C., Sparks, D.L., 2020b. Iron(III) fate after complexation with soil organic matter in fine silt and clay fractions: An EXAFS spectroscopic approach. Soil Tillage Res. 200, 104617. https://doi.org/10.1016/j.still.2020.104617

Ginn, B., Meile, C., Wilmoth, J., Tang, Y., Thompson, A., 2017. Rapid iron reduction rates are stimulated by high-amplitude redox fluctuations in a tropical forest soil. Environ. Sci. Technol. 51, 3250–3259. https://doi.org/10.1021/acs.est.6b05709

Hall, S.J., Berhe, A.A., Thompson, A., 2018. Order from disorder: do soil organic matter composition and turnover co-vary with iron phase crystallinity? Biogeochemistry 140, 93–110. https://doi.org/10.1007/s10533-018-0476-4

Henderson, R., Kabengi, N., Mantripragada, N., Cabrera, M., Hassan, S., Thompson, A., 2012. Anoxia-induced release of colloid- and nanoparticle-bound phosphorus in grassland soils. Environ. Sci. Technol. 46, 11727–11734. https://doi.org/10.1021/es302395r

Hoving, A.L., Sander, M., Bruggeman, C., Behrends, T., 2017. Redox properties of clay-rich sediments as assessed by mediated electrochemical analysis: Separating pyrite, siderite and structural Fe in clay minerals. Chemical Geology, 457, 149-161. https://doi.org/10.1016/j.chemgeo.2017.03.022

Huang, W., Hall, S.J., 2017. Elevated moisture stimulates carbon loss from mineral soils by releasing protected organic matter. Nat. Commun. 8, 1774. https://doi.org/10.1038/s41467-017-01998-z

Huang, X., Tang, H., Kang, W., Yu, G., Ran, W., Jianping Hong, J., Shen, Q., 2018. Redox interface-associated organo-mineral interactions: A mechanism for C sequestration under a rice-wheat cropping system. Soil Biol. Biochem. 120, 12-23. https://doi.org/10.1016/j.soilbio.2018.01.031

Huang, X., Kang, W., Guo, J., Wang, L., Tang, H., Li, T., Yu, G., Ran, W., Hong, J., Shen, Q., 2020. Highly reactive nanomineral assembly in soil colloids: implications for paddy soil carbon

storage. Sci. Total Environ. 703, 134728. https://doi.org/10.1016/j.scitotenv.2019.134728

Kalbitz, K., Kaiser, K., Fiedler, S., Kölbl, A., Amelung, W., Bräuer, T., Cao, Z., Don, A., Grootes, P., Jahn, R., Schwark, L., Vogelsang, V., Wissing, L., Kögel-Knabner, I., 2013. The carbon count of 2000 years of rice cultivation. Glob. Chang. Biol. 19, 1107–1113. https://doi.org/10.1111/gcb.12080

Karlsson, T., Persson, P., 2010. Coordination chemistry and hydrolysis of Fe(III) in a peat humic acid studied by X-ray absorption spectroscopy. Geochim. Cosmochim. Acta 74, 30–40. https://doi.org/10.1016/j.gca.2009.09.023

Kirk, G. 2004. The Biogeochemistry of Submerged Soils. John Wiley & Sons, Chichester, U.K. 291 pp. ISBN 0-470-86301-3.

Kögel-Knabner, I., Amelung, W., Cao, Z., Fiedler, S., Frenzel, P., Jahn, R., Kalbitz, K., Kölbl, A., Schloter, M., 2010. Biogeochemistry of paddy soils. Geoderma 157, 1–14. https://doi.org/10.1016/j.geoderma.2010.03.009

Kölbl, A., Schad, P., Jahn, R., Amelung, W., Bannert, A., Cao, Z.H., Fiedler, S., Kalbitz, K., Lehndorff, E., Müller-Niggemann, C., Schloter, M., Schwark, L., Vogelsang, V., Wissing, L., Kögel-Knabner, I., 2014. Accelerated soil formation due to paddy management on marshlands (Zhejiang Province, China). Geoderma 228–229, 67–89. https://doi.org/10.1016/j.geoderma.2013.09.005

Kramer, M.G., Chadwick, O.A., 2018. Climate-driven thresholds in reactive mineral retention of soil carbon at the global scale. Nat. Clim. Chang. 8, 1104–1108. https://doi.org/10.1038/s41558-018-0341-4

Kramer, M.G., Sanderman, J., Chadwick, O.A., Chorover, J., Vitousek, P.M., 2012. Long-term carbon storage through retention of dissolved aromatic acids by reactive particles in soil. Glob. Chang. Biol. 18, 2594–2605. https://doi.org/10.1111/j.1365-2486.2012.02681.x

Lalonde, K., Mucci, A., Ouellet, A., Gélinas, Y., 2012. Preservation of organic matter in sediments promoted by iron. Nature 483, 198–200. https://doi.org/10.1038/nature10855

Liao, W., Yuan, S., Liu, X., Tong, M., 2019. Anoxic storage regenerates reactive Fe(II) in reduced nontronite with short-term oxidation. Geochim. Cosmochim. Acta 257, 96–109. https://doi.org/10.1016/j.gca.2019.04.027

Mehra, O.P., Jackson, M.L., 1960. Iron oxide removal from soils and clays by dithionite–citrate systems buffered with sodium bicarbonate. Clay Clay Miner. 7, 317–327. https://doi.org/10.1016/B978-0-08-009235-5.50026-7

Neumann, A., Wu, L., Li, W., Beard, B.L., Johnson, C.M., Rosso, K.M., Frierdich, A.J., Scherer, M.M., 2015. Atom exchange between aqueous Fe(II) and structural Fe in clay minerals. Environ. Sci. Technol. 49, 2786–2795. https://doi.org/10.1021/es504984q

O'Day, P.A., Rivera, N., Root, R., Carroll, S.A., 2004. X-ray absorption spectroscopic study of Fe reference compounds for the analysis of natural sediments. Am. Mineral. 89, 572–585. https://doi.org/10.2138/am-2004-0412

Oades, J.M., Waters, A.G., 1991. Aggregate hierarchy in soils. Aust. J. Soil Res. 29, 815–825. https://doi.org/10.1071/SR9910815

Pan, G., Li, L., Wu, L., Zhang, X., 2004. Storage and sequestration potential of topsoil organic carbon in China's paddy soils. Glob. Chang. Biol. 10, 79–92. https://doi.org/10.1111/j.1365-2486.2003.00717.x

Prietzel, J., Thieme, J., Eusterhues, K., Eichert, D., 2007. Iron speciation in soils and soil aggregates

by synchrotron-based X-ray microspectroscopy (XANES, μ-XANES). Eur. J. Soil Sci. 58, 1027–1041. https://doi.org/10.1111/j.1365-2389.2006.00882.x

Prietzel, J., Tyufekchieva, N., Eusterhues, K., Kögel-Knabner. I., Thienme, J., Paterson, D., McNulty, I., de Jonge, M., Eichert, D., Salomé, M., 2009. Anoxic versus oxic sample pretreatment: effects on the speciation of sulfur and iron in well-areated and wetland soils as assessed by X-ray absorption near-edge spectroscopy (XANES). Geoderma 153, 318-330. https://doi.org/10.1016/j/geoderma.2009.08.015

Ribeiro, F.R., Fabris, J.D., Kostka, J.E., Komadel, P., Stucki, J.W., 2009. Comparisons of structural iron reduction in smectites by bacteria and dithionite: II. A variable-temperature Mössbauer spectroscopic study of Garfield nontronite. Pure Appl. Chem. 81, 1499–1509. https://doi.org/10.1351/PAC-CON-08-11-16

Riedel, T., Zak, D., Biester, H., Dittmar, T., 2013. Iron traps terrestrially derived dissolved organic matter at redox interfaces. Proc. Natl. Acad. Sci. U. S. A. 110, 10101–10105. https://doi.org/10.1073/pnas.1221487110

Rothwell, K., Kretzschmar, R., 2020. Siderite oxidation in the presence of organic ligands. EGU General Assembly 2020-16894. https://doi.org/10.5194/egusphere-egu2020-16894

Said-Pullicino, D., Giannetta, B., Demeglio, B., Missong, A., Gottselig, N., Romani, M., Bol, R., Klumpp, E., Celi, L., 2021. Redox-driven changes in water-dispersible colloids and their role in carbon cycling in hydromorphic soils. Geoderma 385, 114894. https://doi.org/10.1016/j.geoderma.2020.114894

Said-Pullicino, D., Miniotti, E.F., Sodano, M., Bertora, C., Lerda, C., Chiaradia, E.A., Romani, M., Cesari de Maria, S., Sacco, D., Celi, L., 2016. Linking dissolved organic carbon cycling to organic carbon fluxes in rice paddies under different water management practices. Plant Soil 401, 273–290. https://doi.org/10.1007/s11104-015-2751-7

Sawrat K.L. (2004) Organic matter accumulation in submerged soils. Adv. Agron. 81, 169–201.

Schwertmann, U., 1964. Differenzierung der Eisenoxide des Bodens durch Extraktion mit saurer Ammonium-oxalat Lösung. Z Pflanzenernaehr Dueng Bodenkd 105, 194–202.

Shelobolina, E., Konishi, H., Xu, H., Benzine, J., Xiong, M.Y., Wu, T., Blöthe, M., Roden, E., 2012. Isolation of phyllosilicate-iron redox cycling microorganisms from an llite-smectite rich hydromorphic soil. Front. Microbiol. 3, 1–10. https://doi.org/10.3389/fmicb.2012.00134

Shi, B., Smeaton, C., Roden, E., Lee, S., Liu, K., Xu, H., Kendall, B., Johnson, C., Parsons, C.T., Van Cappellen, P., 2021. Consecutive Fe redox cycles decrease bioreducible Fe(III) and Fe isotope fractions by eliminating small clay particles. Geochim. Cosmochim. Acta 308, 118-135. https://doi.org/10.1016/j.gca.2021.05.040

Six, J., Elliott, E.T., Paustian, K., 2000. Soil macroaggregate turnover and microaggregate formation: A mechanism for C sequestration under no-tillage agriculture. Soil Biol. Biochem. 32, 2099–2103. https://doi.org/10.1016/S0038-0717(00)00179-6

Sodano, M., Lerda, C., Nisticò, R., Martin, M., Magnacca, G., Celi, L., Said-Pullicino, D., 2017. Dissolved organic carbon retention by coprecipitation during the oxidation of ferrous iron. Geoderma 307, 19–29. https://doi.org/10.1016/j.geoderma.2017.07.022

Sodano, M., Said-Pullicino, D., Fiori, A.F., Catoni, M., Martin, M., Celi, L., 2016. Sorption of paddy soil-derived dissolved organic matter on hydrous iron oxide-vermiculite mineral phases. Geoderma 261, 169–177. https://doi.org/10.1016/j.geoderma.2015.07.014

Thompson, A., Chadwick, O.A., Boman, S., Chorover, J., 2006. Colloid mobilization during soil iron

redox oscillations. Environ. Sci. Technol. 40, 5743–5749. https://doi.org/10.1021/es061203b

Torn, M.S., Trumbore, S.E., Chadwick, O.A., Vitousek, P.M., Hendricks, D.M., 1997. Mineral control of soil organic carbon storage and turnover content were measured by horizon down to the depth at which. Nature 389, 3601–3603. https://doi.org/10.1038/38260

Totsche, K.U., Amelung, W., Gerzabek, M.H., Guggenberger, G., Klumpp, E., Knief, C., Lehndorff, E., Mikutta, R., Peth, S., Prechtel, A., Ray, N., Kögel-Knabner, I., 2018. Microaggregates in soils. J. Plant Nutr. Soil Sci. 181, 104–136. https://doi.org/10.1002/jpln.201600451

Vogelsang, V., Fiedler, S., Jahn, R., Kaiser, K., 2016. In-situ transformation of iron-bearding minerals in marshland-derived paddy subsoil. Eur. J. Soil Sci. 67, 676-685. https://doi.org/10.1111/ejss.12374

Westre, T.E., Kennepohl, P., DeWitt, J.G., Hedman, B., Hodgson, K.O., Solomon, E.I., 1997. A multiplet analysis of Fe K-edge 1s → 3d pre-Edge features of iron complexes. J. Am. Chem. Soc. 119, 6297–6314. https://doi.org/10.1021/ja964352a

Wilke, M., Farges, F., Petit, P.E., Brown, G.E., Martin, F., 2001. Oxidation state and coordination of Fe in minerals: An Fe K-XANES spectroscopic study. Am. Mineral. 86, 714–730. https://doi.org/10.2138/am-2001-5-612

Winkler, P., Kaiser, K., K¨olbl, A., Kühn, T., Schad, P., Urbanski, L., Fiedler, S., Lehndorff, E., Kalbitz, K., Utami, S.R., Cao, Z., Zhang, G., Jahn, R., Kögel-Knabner, I., 2016. Response of Vertisols, Andosols, and Alisols to paddy management. Geoderma 261, 23–35. https://doi.org/10.1016/j.geoderma.2015.06.017

Winkler, P., Kaiser, K., Jahn, R., Mikutta, R., Fiedler, S., Cerli, C., Kölbl, A., Schulz, S., Jankowska, M., Schloter, M., Müller-Niggemann, C., Schwark, L., Woche, S.K., Kümmel, S., Utami, S.R., Kalbitz, K., 2019. Tracing organic carbon and microbial community structure in mineralogically different soils exposed to redox fluctuations. Biogeochemistry 143, 31–54. https://doi.org/10.1007/s10533-019-00548-7

Wissing, L., Kölbl, A., Häusler, W., Schad, P., Cao, Z.H., Kögel-Knabner, I., 2013. Management-induced organic carbon accumulation in paddy soils: The role of organo-mineral associations. Soil Tillage Res. 126, 60–71. https://doi.org/10.1016/j.still.2012.08.004

Wissing, L., Kölbl, A., Schad, P., Bräuer, T., Cao, Z.H., Kögel-Knabner, I., 2014. Organic carbon accumulation on soil mineral surfaces in paddy soils derived from tidal wetlands. Geoderma 228–229, 90–103. https://doi.org/10.1016/j.geoderma.2013.12.012

Wissing, L., Kölbl, A., Vogelsang, V., Fu, J.R., Cao, Z.H., Kögel-Knabner, I., 2011. Organic carbon accumulation in a 2000-year chronosequence of paddy soil evolution. Catena 87, 376–385. https://doi.org/10.1016/j.catena.2011.07.007

Xue, B., Huang, L., Huang, Y., Zhou, F., Li, F., Kubar, K.A., Li, X., Lu, J., Zhu, J., 2019. Roles of soil organic carbon and iron oxides on aggregate formation and stability in two paddy soils. Soil Tillage Res. 187, 161–171. https://doi.org/10.1016/j.still.2018.12.010

Zhang, G., Burgos, W.D., Senko, J.M., Bishop, M.E., Dong, H., Boyanov, M.I., Kemner, K.M., 2011. Microbial reduction of chlorite and uranium followed by air oxidation. Chemical Geology 283, 242–250. https://doi.org/10.1016/j.chemgeo.2011.01.021

Zhao, L., Dong, H., Kukkadapu, R., Agrawal, A., Liu, D., Zhang, J., Edelmann, R.E., 2013. Biological oxidation of Fe(II) in reduced nontronite coupled with nitrate reduction by *Pseudogulbenkiania* sp. Strain 2002. Geochim. Cosmochim. Acta 119, 231–247. https://doi.org/10.1016/j.gca.2013.05.033

Figure captions

Figure 1. Soil OC distribution between different aggregate and particle-size fractions in in the (a) non-paddy and (b) paddy soils as a function of soil depth. CSa+POM, coarse sand and particulate OM; FSa, fine sand; CSi, coarse silt; FSi, fine silt; Cl, clay. Black bars represent the proportion of fraction OC within microaggregates for the coarse silt (mCSi), fine silt (mFSi), and clay (mCl) fractions. Error bars represent the standard error.

Figure 2. Intra:inter-microaggregate ratio of (a) OC and (b) pedogenic Fe (Fe_d) associated with coarse silt (CSi), fine silt (FSi), and clay (Cl) particle-size fractions as a function of depth for non-paddy and paddy soils.

Figure 3. Distribution of dithionite-citrate-bicarbonate-extractable Fe (Fe_d; a, b), oxalate-extractable Fe (Fe_o; c, d), and crystalline Fe (hyr)oxides (Fe_c; e, f) between different aggregate and particle-size fractions in the non-paddy (a, c, e) and paddy (b, d, f) soils as a function of soil depth. CSa+POM, coarse sand and particulate OM; FSa, fine sand; CSi, coarse silt; FSi, fine silt; Cl, clay. Black bars represent the proportion of fraction pedogenic Fe within microaggregates for the coarse silt (mCSi), fine silt (mFSi), and clay (mCl) fractions.

Figure 4. Changes in the Fe-K edge XANES pre-edge centroid position for (a) fine sand (FSa), inter and intra-microaggregate coarse silt (CSi and mCSi), (b) inter and intra-microaggregate fine silt (FSi and mFSi), and (c) inter and intra-microaggregate clay (Cl and mCl) fractions in non-paddy and paddy soils as a function of soil depth.

Figure 5. k^3-weighted EXAFS spectra of the coarse silt (CSi), fine silt (FSi), clay (Cl), coarse silt in aggregates (mCSi), fine silt in aggregates (mFSi), clay in aggregates (mCl) fractions of Ap1, Ap2, Bgw horizons of non-paddy soil and Arp1, Arp2, Arpd, Brd1 and Brd2 horizons of paddy soil. The red dotted lines represent the linear combination fits of the sample spectra (n=3). R-factors for the fits are displayed.

Figure 6. High-resolution WT plots of of the coarse silt (CSi), fine silt (FSi), clay (Cl), coarse silt in aggregates (mCSi), fine silt in aggregates (mFSi), clay in aggregates (mCl) fractions of non- paddy (a) and paddy (b) soils. Data are plotted as a function of k ($Å^{-1}$)

on the x axis and R (Å) on the y axis in the range 2.2−4.0 (Å).

Figure 1

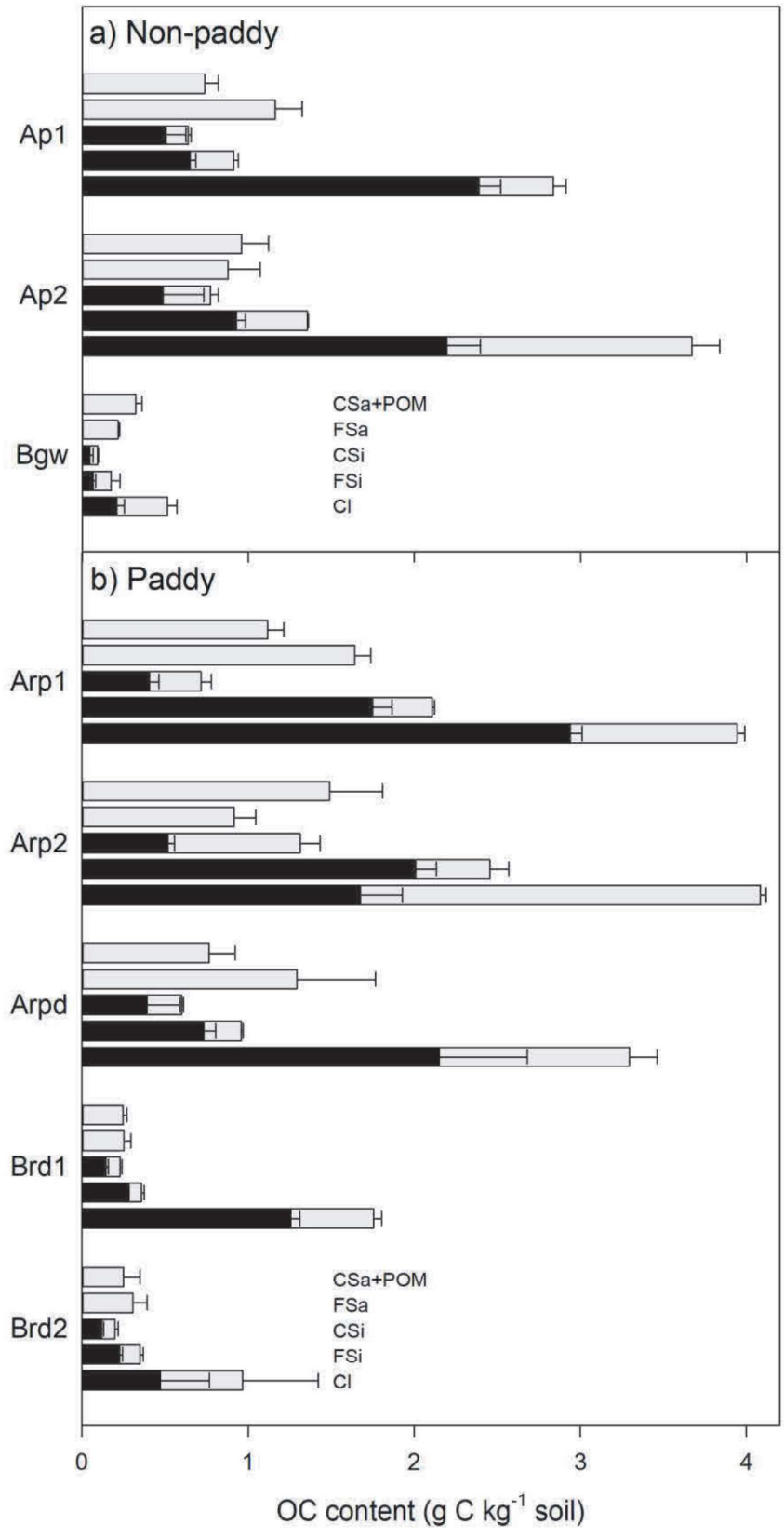
a) Non-paddy
Ap1
Ap2
Bgw
CSa+POM
FSa
CSi
FSi
CI
b) Paddy
Arp1
Arp2
Arpd
Brd1
Brd2
CSa+POM
FSa
CSi
FSi
CI
0
1
2
3
4
OC content (g C kg-1 soil)

Figure 2

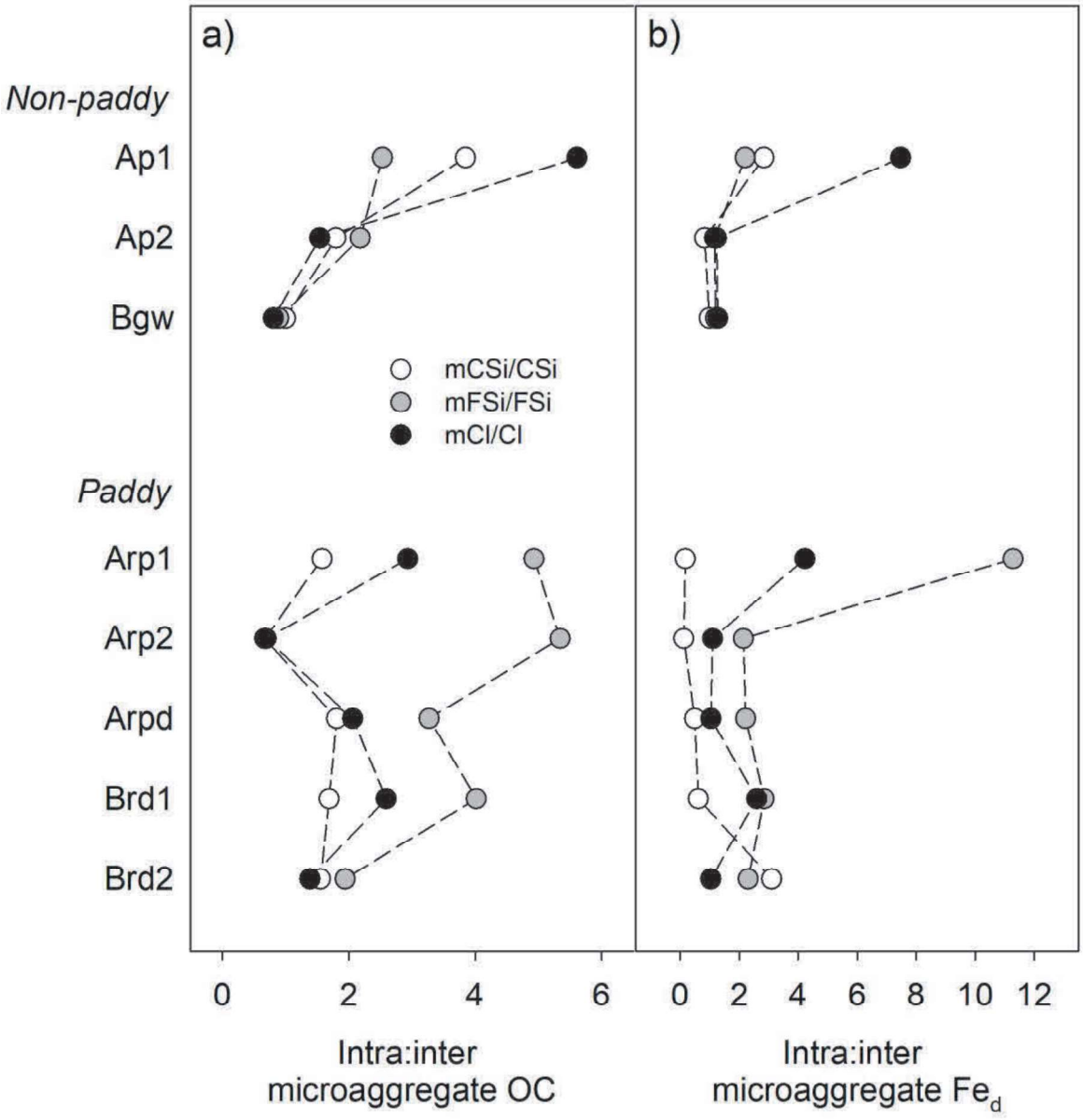
a)
b)
Non-paddy
Ap1
Ap2
Bgw
mCSi/CSi
mFSi/FSi
mCl/Cl
Paddy
Arp1
Arp2
Arpd
Brd1
Brd2
0
2
4
6
0
2
4
6
8
10
12
Intra:inter microaggregate OC
Intra:inter microaggregate Fe$_d$

Figure 3

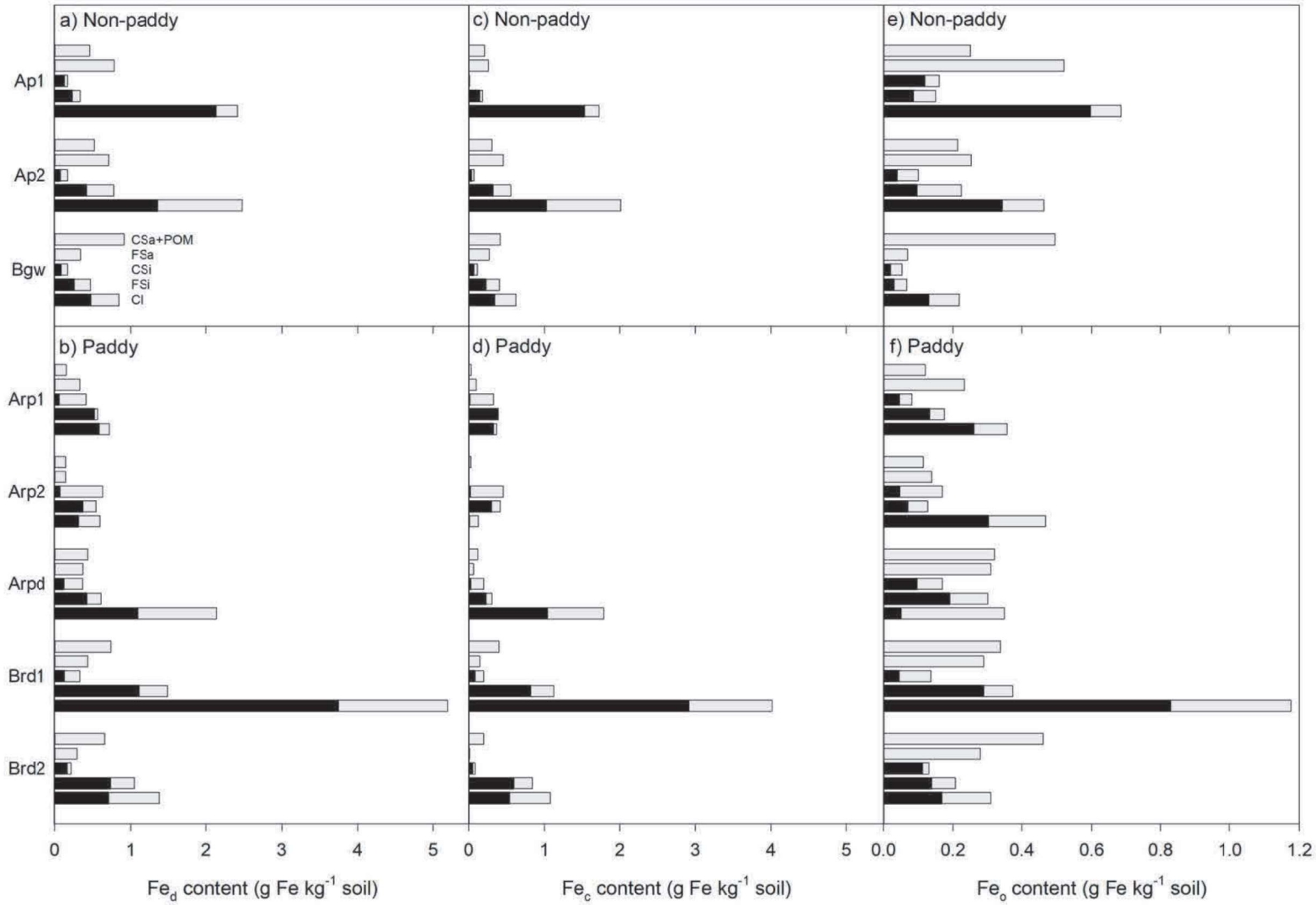
a) Non-paddy
c) Non-paddy
e) Non-paddy
b) Paddy
d) Paddy
f) Paddy
Ap1
Ap2
Bgw
Arp1
Arp2
Arpd
Brd1
Brd2
CSa+POM
FSa
CSi
FSi
CI
0
1
2
3
4
5
0.0
0.2
0.4
0.6
0.8
1.0
1.2
Fe$_d$ content (g Fe kg^{-1} soil)
Fe$_c$ content (g Fe kg^{-1} soil)
Fe$_o$ content (g Fe kg^{-1} soil)

Figure 4

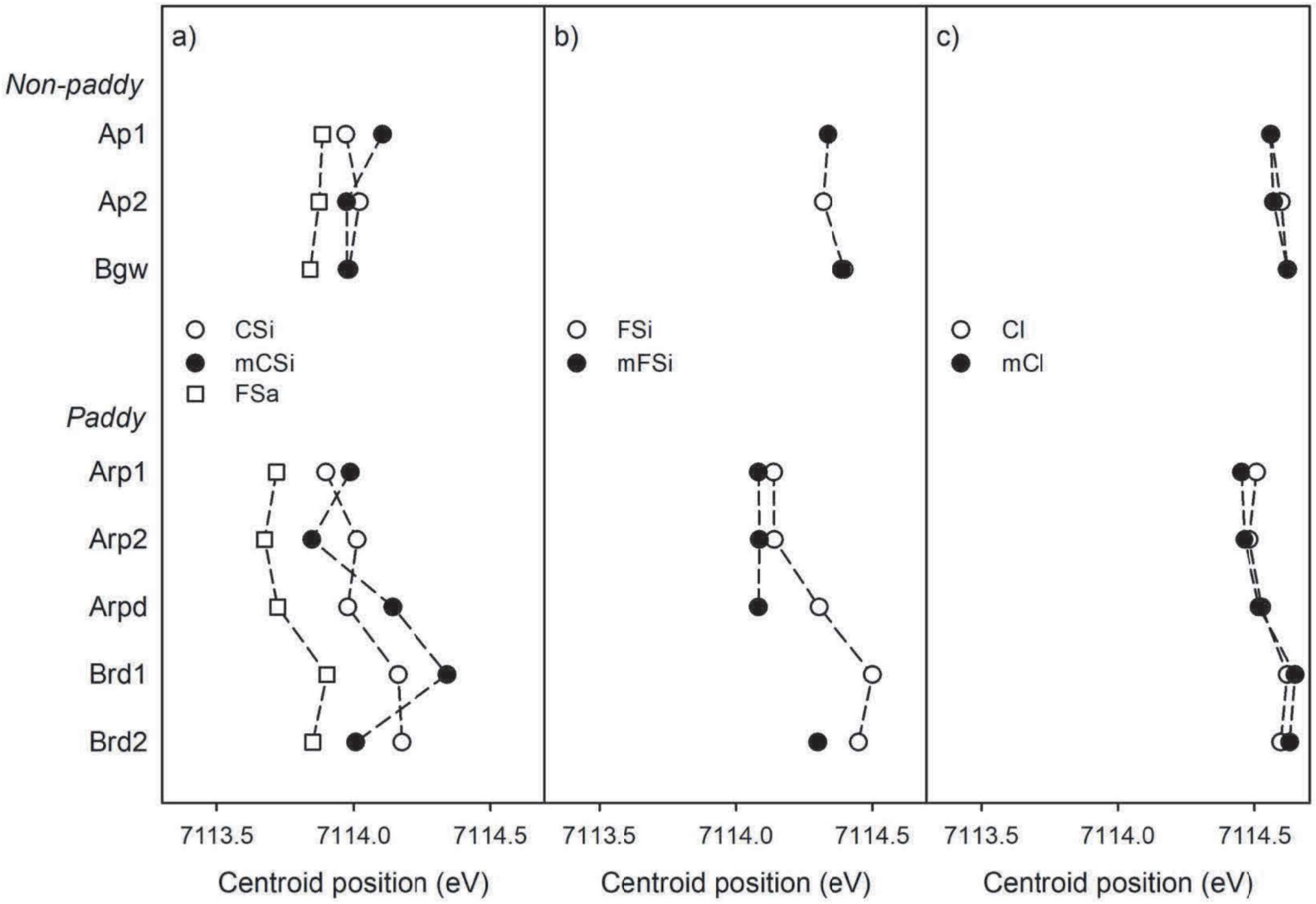
a)
b)
c)
Non-paddy
Ap1
Ap2
Bgw
CSi
mCSi
FSa
FSi
mFSi
Cl
mCl
Paddy
Arp1
Arp2
Arpd
Brd1
Brd2
7113.5
7114.0
7114.5
Centroid position (eV)

Figure 5

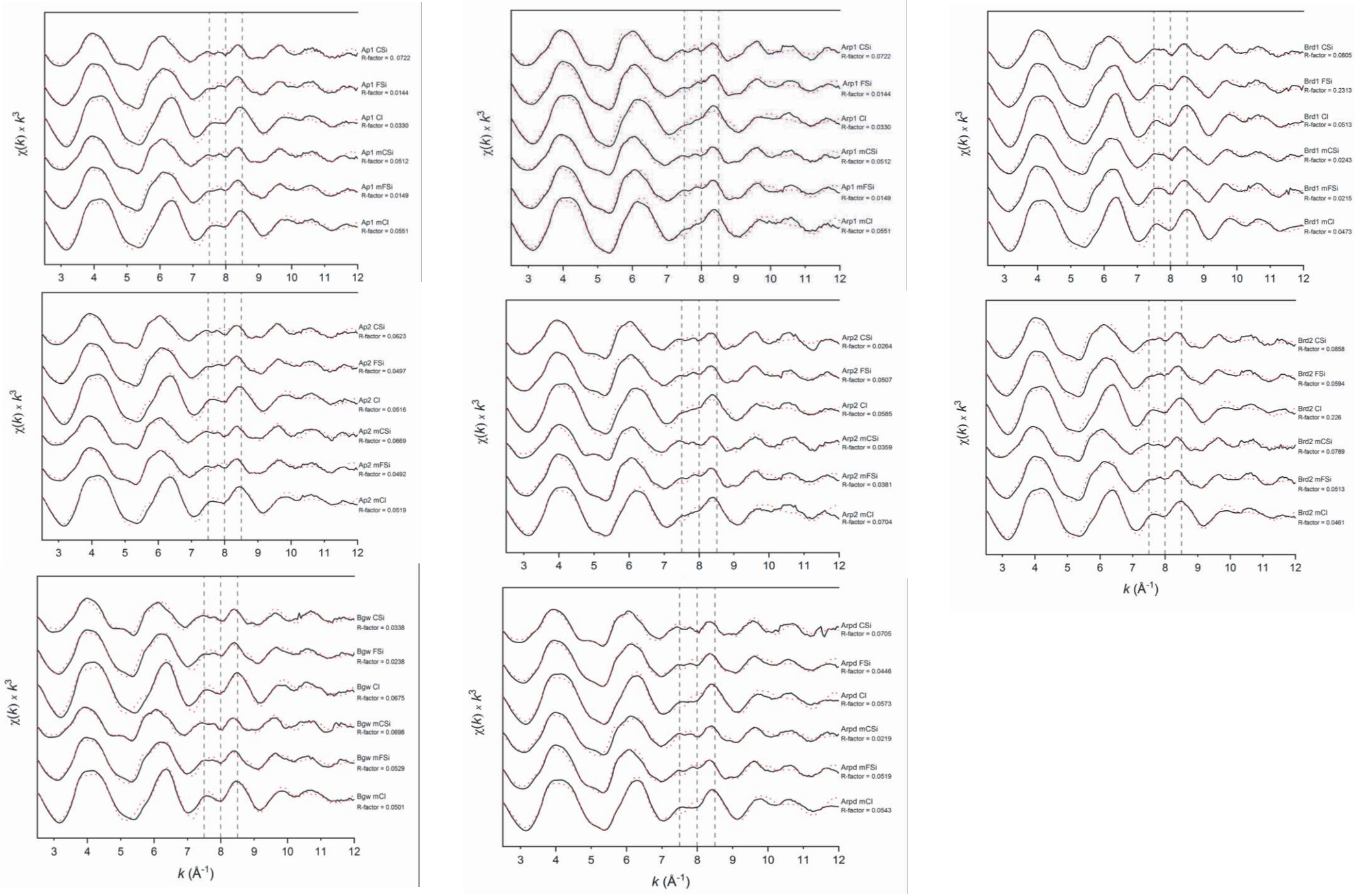
Ap1 CSi
R-factor = 0. 0722
Ap1 FSi
R-factor = 0.0144
Ap1 Cl
R-factor = 0.0330
Ap1 mCSi
R-factor = 0.0512
Ap1 mFSi
R-factor = 0.0149
Ap1 mCl
R-factor = 0.0551
Ap2 CSi
R-factor = 0.0623
Ap2 FSi
R-factor = 0.0497
Ap2 Cl
R-factor = 0.0516
Ap2 mCSi
R-factor = 0.0669
Ap2 mFSi
R-factor = 0.0492
Ap2 mCl
R-factor = 0.0519
Bgw CSi
R-factor = 0.0338
Bgw FSi
R-factor = 0.0238
Bgw Cl
R-factor = 0.0675
Bgw mCSi
R-factor = 0.0698
Bgw mFSi
R-factor = 0.0529
Bgw mCl
R-factor = 0.0501
Arp1 CSi
R-factor = 0.0722
Arp1 FSi
R-factor = 0.0144
Arp1 Cl
R-factor = 0.0330
Arp1 mCSi
R-factor = 0.0512
Ap1 mFSi
R-factor = 0.0149
Arp1 mCl
R-factor = 0.0551
Arp2 CSi
R-factor = 0.0264
Arp2 FSi
R-factor = 0.0507
Arp2 Cl
R-factor = 0.0585
Arp2 mCSi
R-factor = 0.0359
Arp2 mFSi
R-factor = 0.0381
Arp2 mCl
R-factor = 0.0704
Arpd CSi
R-factor = 0.0705
Arpd FSi
R-factor = 0.0446
Arpd Cl
R-factor = 0.0573
Arpd mCSi
R-factor = 0.0219
Arpd mFSi
R-factor = 0.0519
Arpd mCl
R-factor = 0.0543
Brd1 CSi
R-factor = 0.0805
Brd1 FSi
R-factor = 0.2313
Brd1 Cl
R-factor = 0.0513
Brd1 mCSi
R-factor = 0.0243
Brd1 mFSi
R-factor = 0.0215
Brd1 mCl
R-factor = 0.0473
Brd2 CSi
R-factor = 0.0858
Brd2 FSi
R-factor = 0.0594
Brd2 Cl
R-factor = 0.226
Brd2 mCSi
R-factor = 0.0789
Brd2 mFSi
R-factor = 0.0513
Brd2 mCl
R-factor = 0.0461
χ(k) x k3
k (Å-1)
3 4 5 6 7 8 9 10 11 12

Figure 6

a)

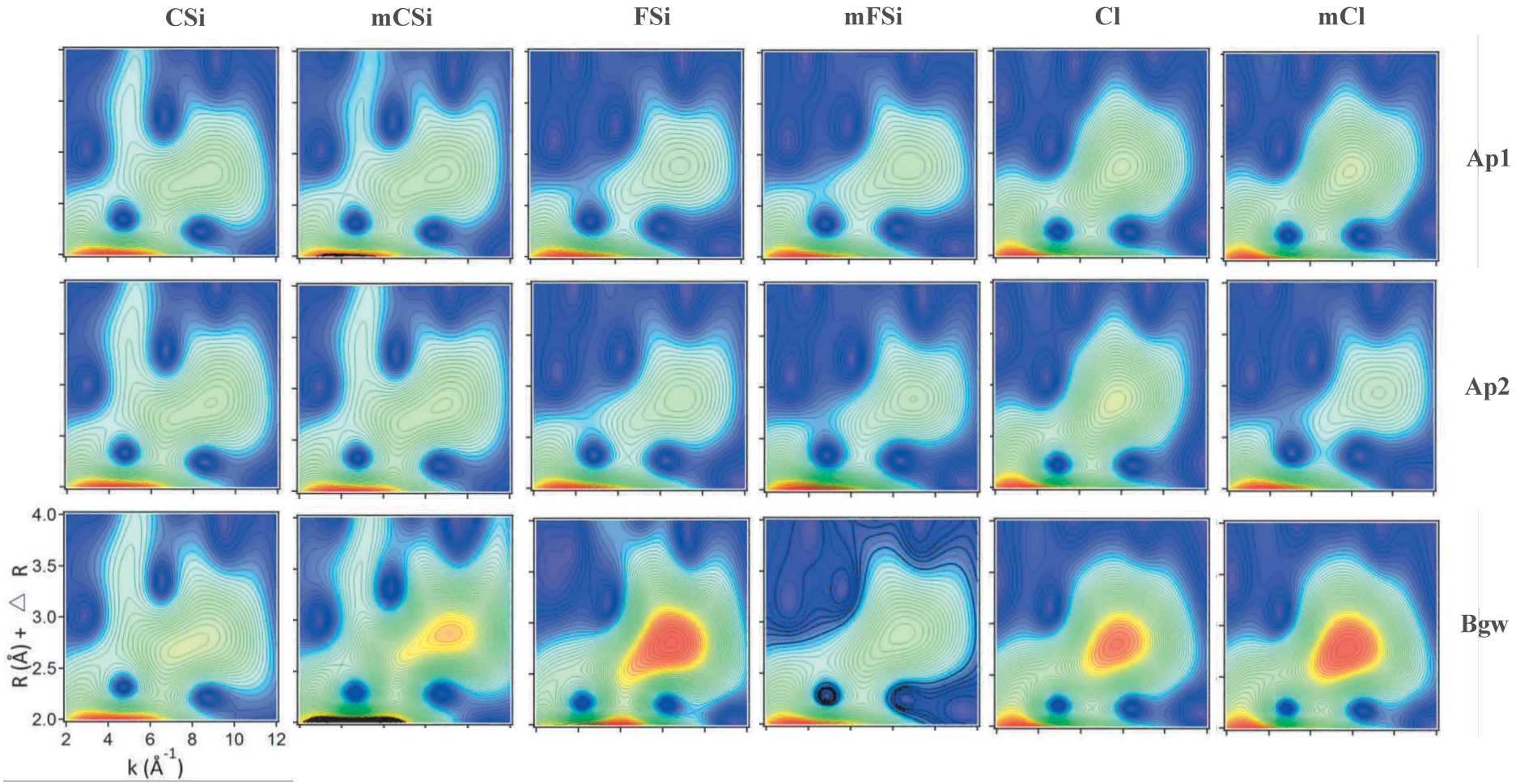
CSi
mCSi
FSi
mFSi
Cl
mCl
Ap1
Ap2
Bgw
R (Å) + △ R
4.0
3.5
3.0
2.5
2.0
2
4
6
8
10
12
k (Å-1)

b)

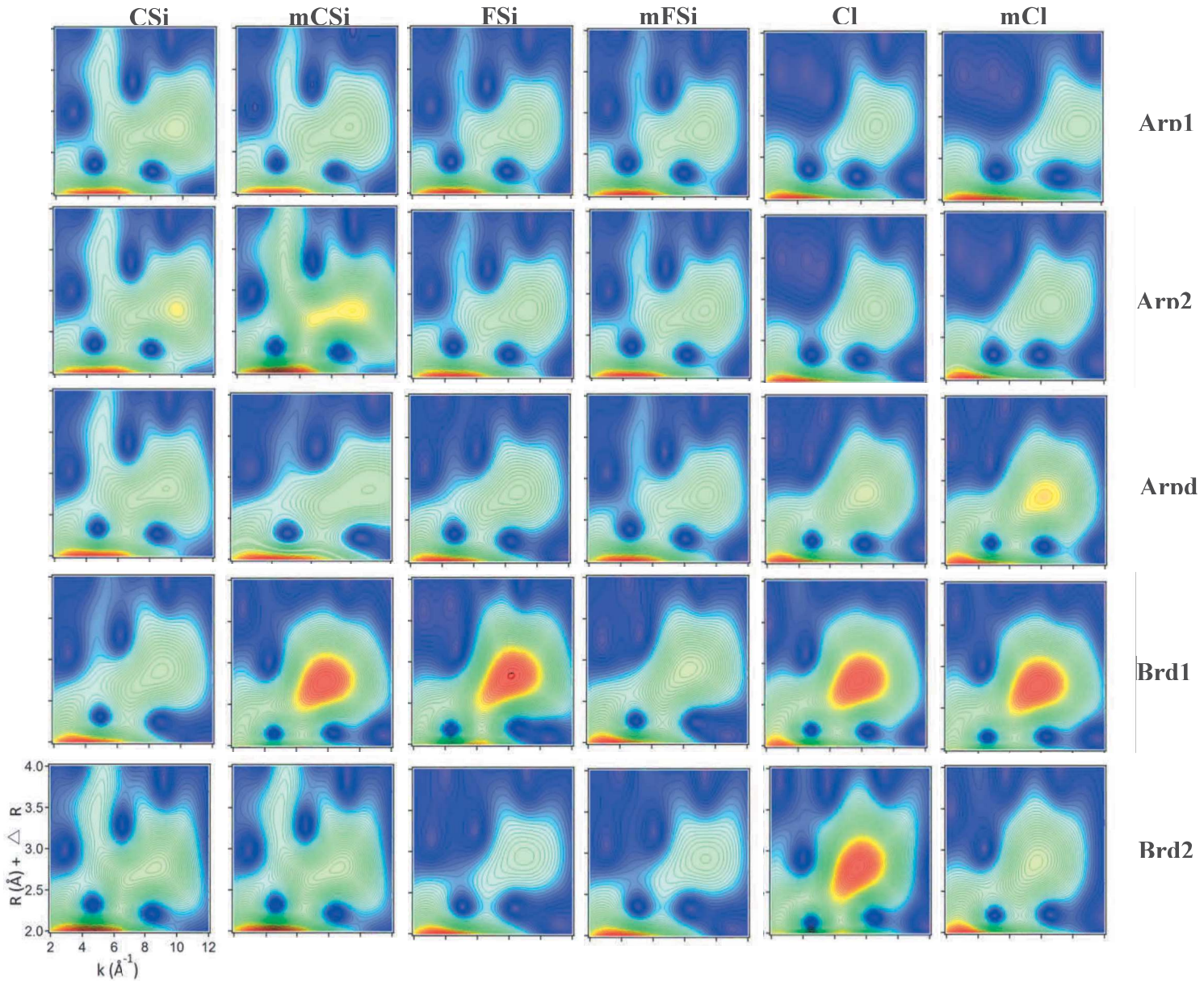
CSi
mCSi
FSi
mFSi
Cl
mCl
Arn1
Arn2
Arnd
Brd1
Brd2
R (Å) + △ R
4.0
3.5
3.0
2.5
2.0
2
4
6
8
10
12
k (Å-1)

Table 1. Ratio of oxalate-extractable Fe (Fe_o) to dithionite-citrate-bicarbonate-extractable Fe (Fe_d) in different particle-size fractions for each horizon in the non-paddy and paddy soils.

Soil/Horizon	CSa+POM	FSa	CSi + mCSi	FSi + mFSi	Cl + mCl
Non-paddy					
Ap1	0.5	0.7	0.9	0.4	0.3
Ap2	0.4	0.4	0.6	0.3	0.2
Bgw	0.5	0.2	0.3	0.1	0.3
Paddy					
Arp1	0.8	0.7	0.2	0.3	0.5
Arp2	0.8	1.0	0.3	0.2	0.8
Arpd	0.7	0.8	0.5	0.5	0.2
Brd1	0.5	0.7	0.4	0.3	0.2
Brd2	0.7	1.0	0.6	0.2	0.2

CSa+POM, coarse sand and particulate OM; FSa, fine sand; CSi, inter-microaggregate coarse silt; mCSi, intra-microaggregate coarse silt; FSi, inter-microaggregate fine silt; mFSi, intra-microaggregate fine silt; Cl, inter-microaggregate clay; mCl, intra-microaggregate clay fraction.

Table 2. Results for the LCF performed on the Fe K-edge XANES data of the fine sand (FSa), coarse silt (CSi), fine silt (FSi), clay (Cl), coarse silt in aggregates (mCSi), fine silt in aggregates (mFSi), clay in aggregates (mCl) fractions of Ap1, Ap2, Bgw horizons of non-paddy soil and Arp1, Arp2, Arpd, Brd1, and Brd2 horizons of paddy soil.

	Chi2	Component 1	%	Component 2	%	Component 3	%	Component 4	%	Sum
Ap1 FSa	0.033087096	Chlorite	32	Siderite	26	Illite	21	Hematite	20	100
Ap1 CSi	0.019310413	Chlorite	26	Illite	48	Hematite	21	Magnetite	5	100
Ap1 mCSi	0.008858912	Chlorite	22	Illite	66	Hematite	13			100
Ap1 FSi	0.008196354	Chlorite	27	Smectite	42	Nontronite	19	Lepidocrocite	11	100
Ap1 mFSi	0.006696096	Chlorite	26	Smectite	47	Illite	23	FeIII citrate	4	100
Ap1 Cl	0.010688951	Chlorite	8	Jacobsite	13	Nontronite	79			100
Ap1 mCl	0.010184488	Chlorite	8	Jacobsite	13	Nontronite	79			100
Ap2 FSa	0.039485435	Chlorite	33	Siderite	33	Illite	13	Hematite	20	100
Ap2 CSi	0.022535003	Chlorite	27	Illite	46	Hematite	27			100
Ap2 mCSi	0.027156644	Chlorite	26	Illite	37	Hematite	23	Magnetite	14	100
Ap2 FSi	0.006497925	Chlorite	25	Illite	26	Smectite	42	FeIII citrate	7	100
Ap2 mFSi	0.427969307	Chlorite	12	Jacobsite	38	Nontronite	50			100
Ap2 Cl	0.009034114	Chlorite	11	Smectite	65	Lepidocrocite	24			100
Ap2 mCl	0.013101914	Chlorite	11	Nontronite	84	Lepidocrocite	5			100
Bgw FSa	0.038458154	Chlorite	34	Siderite	29	Illite	14	Hematite	22	100
Bgw CSi	0.032032481	Chlorite	26	Illite	36	Hematite	27	Magnetite	11	100
Bgw mCSi	0.026492885	Chlorite	25	Illite	34	Hematite	26	Magnetite	14	100
Bgw FSi	0.007402408	Chlorite	26	Smectite	61	Goethite	9	FeIII citrate	4	100
Bgw mFSi	0.007050961	Chlorite	23	Smectite	25	Illite	42	FeIII citrate	9	100
Bgw Cl	0.013186125	Chlorite	8	Nontronite	77	Ferrihydrite	15			100

Bgw mCl	0.014873833	Chlorite	10	Nontronite	83	FeIII citrate	7			100
Arp1 FSa	0.027628912	Chlorite	33	Siderite	29	Illite	19	Hematite	18	100
Arp1 CSi	0.01276442	Chlorite	27	Illite	64	Magnetite	9			100
Arp1 mCSi	0.009723367	Chlorite	24	Illite	68	Hematite	9			100
Arp1 FSi	0.009919808	Chlorite	29	Illite	26	Smectite	22	Nontronite	22	100
Arp1 mFSi	0.008831991	Chlorite	29	Illite	42	Smectite	22	Nontronite	7	100
Arp1 Cl	0.010773327	Chlorite	19	Smectite	80	FeIII citrate	1			100
Arp1 mCl	0.010542052	Chlorite	16	Jacobsite	5	Nontronite	79			100
Arp2 FSa	0.034934128	Chlorite	33	Siderite	32	Hematite	22	Magnetite	13	100
Arp2 CSi	0.01158174	Chlorite	27	Illite	60	Hematite	11	Magnetite	2	100
Arp2 mCSi	0.047753368	Chlorite	26	Illite	40	Magnetite	34			100
Arp2 FSi	0.00624999	Chlorite	26	Illite	52	Smectite	22			100
Arp2 mFSi	0.006762771	Chlorite	26	Illite	58	Smectite	16			100
Arp2 Cl	0.008425091	Chlorite	19	Smectite	74	Lepidocrocite	7			100
Arp2 mCl	0.007167858	Chlorite	18	Smectite	65	Ferrihydrite	17			100
Arpd FSa	0.032190435	Chlorite	34	Siderite	32	Illite	14	Hematite	20	100
Arpd CSi	0.017333956	Chlorite	27	Illite	47	Hematite	18	Magnetite	8	100
Arpd mCSi	0.005592672	Chlorite	19	Illite	75	Fe III citrate	6			100
Arpd FSi	0.007043644	Chlorite	28	Smectite	33	Nontronite	25	Goethite	14	100
Arpd mFSi	0.008959662	Chlorite	28	Illite	44	Smectite	21	Nontronite	7	100
Arpd Cl	0.008911101	Chlorite	12	Jacobsite	11	Nontronite	78			100
Arpd mCl	0.009600908	Chlorite	11	Jacobsite	12	Nontronite	77			100
Brd1 FSa	0.029485302	Chlorite	32	Siderite	27	Illite	19	Hematite	22	100
Brd1 CSi	0.008067183	Chlorite	20	Illite	63	Hematite	17			100
Brd1 mCSi	0.004323186	Chlorite	19	Illite	53	Smectite	14	FeIII citrate	14	100
Brd1 FSi	0.005927233	Chlorite	23	Smectite	35	Nontronite	32	FeIII citrate	9	100
Brd1 mFSi	0.066203605	Chlorite		Smectite		Nontronite		FeIII citrate		

Brd1 Cl	0.015676096	Chlorite	10	Nontronite	84	FeIII citrate	6			100
Brd1 mCl	0.014728171	Chlorite	9	Nontronite	83	Fe(III)-citrate	8			100
Brd2 FSa	0.031482016	Chlorite	32	Siderite	31	Illite	16	Hematite	20	100
Brd2 CSi	0.00581651	Chlorite	18	Illite	75	Maghemite	7			100
Brd2 mCSi	0.022010179	Chlorite	25	Illite	39	Hematite	23	Magnetite	12	100
Brd2 FSi	0.008325141	Chlorite	26	Smectite	57	Goethite	17			100
Brd2 mFSi	0.007011355	Chlorite	25	Illite	28	Smectite	40	FeIII citrate	6	100
Brd2 Cl	0.012284473	Chlorite	9	Nontronite	81	Ferrihydrite	11			100
Brd2 mCl	0.010851395	Chlorite	10	Smectite	66	Lepidocrocite	24			100

Table 3. Results for the four-components LCF performed on the k^3- weighted Fe K-edge EXAFS data of the fine sand (FSa) coarse silt (CSi), fine silt (FSi), clay (Cl), coarse silt in aggregates (mCSi), fine silt in aggregates (mFSi), clay in aggregates (mCl) fractions of Ap1, Ap2, Bgw horizons of non-paddy soil and Arp1, Arp2, Arpd, Brd1, and Brd2 horizons of paddy soil. Results are expressed in percentage of the fitting components corresponding to experimental spectra of model compounds reported by O'Day et al. (2004) chlorite, ferrihydrite, lepidocrocite, and Fe(III)-citrate.

	R-factor	Component 1	%	Component 2	%	Component 3		Component 4	%	Sum
Ap1 FSa	0.079749	Chlorite	44	Magnetite	8	Goethite	33	Lepidocrocite	15	100
Ap1 CSi	0.0429419	Chlorite	46	Ferrihydrite	21	Lepidocrocite	17	FeIII citrate	17	100
Ap1 mCSi	0.0343152	Chlorite	44	Ferrihydrite	20	Lepidocrocite	15	FeIII citrate	21	100
Ap1 FSi	0.0339569	Chlorite	35	Ferrihydrite	19	Lepidocrocite	13	FeIII citrate	33	100
Ap1 mFSi	0.0289672	Chlorite	34	Ferrihydrite	22	Lepidocrocite	13	FeIII citrate	31	100
Ap1 Cl	0.0350046	Chlorite	13	Ferrihydrite	31	Lepidocrocite	14	FeIII citrate	43	100
Ap1 mCl	0.0339516	Chlorite	13	Ferrihydrite	31	Lepidocrocite	13	FeIII citrate	42	100
Ap2 FSa	0.0945382	Chlorite	49	Illite	19	Hematite	13	Lepidocrocite	19	100
Ap2 CSi	0.0425902	Chlorite	49	Ferrihydrite	20	Lepidocrocite	16	FeIII citrate	15	100
Ap2 mCSi	0.0529809	Chlorite	49	Ferrihydrite	24	Lepidocrocite	17	FeIII citrate	11	100
Ap2 FSi	0.0316848	Chlorite	35	Ferrihydrite	22	Lepidocrocite	13	FeIII citrate	30	100
Ap2 mFSi	0.0324117	Chlorite	36	Ferrihydrite	21	Lepidocrocite	12	FeIII citrate	31	100
Ap2 Cl	0.0406223	Chlorite	15	Ferrihydrite	36	Lepidocrocite	11	FeIII citrate	38	100
Ap2 mCl	0.0405023	Chlorite	13	Ferrihydrite	35	Lepidocrocite	12	FeIII citrate	40	100
Bgw FSa	0.0561351	Chlorite	47	Illite	14	Hematite	14	Lepidocrocite	25	100
Bgw CSi	0.0293375	Chlorite	48	Ferrihydrite	24	Lepidocrocite	19	Fe III citrate	9	100
Bgw mCSi	0.0565707	Chlorite	48	Ferrihydrite	24	Lepidocrocite	17	Fe III citrate	11	100
Bgw FSi	0.0119554	Chlorite	30	Ferrihydrite	25	Lepidocrocite	15	Fe III citrate	30	100
Bgw mFSi	0.0302615	Chlorite	32	Ferrihydrite	25	Lepidocrocite	14	Fe III citrate	29	100
Bgw Cl	0.0484722	Chlorite	4	Ferrihydrite	42	Lepidocrocite	17	FeIII citrate	37	100

Bgw mCl	0.02219	Chlorite	12	Ferrihydrite	43	Lepidocrocite	15	Fe III citrate	31	100
Arp1 FSa	0.1303528	Chlorite	45	Illite	16	Ferrihydrite	28	Lepidocrocite	12	100
Arp1 CSi	0.0431159	Chlorite	54	Ferrihydrite	8	Lepidocrocite	14	FeIII citrate	23	100
Arp1 mCSi	0.0394779	Chlorite	46	Ferrihydrite	15	Lepidocrocite	16	FeIII citrate	23	100
Arp1 FSi	0.0128322	Chlorite	43	Ferrihydrite	9	Lepidocrocite	13	FeIII citrate	34	100
Arp1 mFSi	0.0117425	Chlorite	45	Ferrihydrite	13	Lepidocrocite	13	FeIII citrate	29	100
Arp1 Cl	0.0513891	Chlorite	26	Ferrihydrite	14	Lepidocrocite	14	FeIII citrate	46	100
Arp1 mCl	0.0461159	Chlorite	25	Ferrihydrite	16	Lepidocrocite	14	FeIII citrate	45	100
Arp2 FSa	0.1116709	Chlorite	50	Magnetite	10	Hematite	13	Lepidocrocite	27	100
Arp2 CSi	0.0604463	Chlorite	51	Ferrihydrite	13	Lepidocrocite	17	FeIII citrate	18	100
Arp2 mCSi	0.0320848	Chlorite	56	Ferrihydrite	16	Lepidocrocite	19	FeIII citrate	9	100
Arp2 FSi	0.0339822	Chlorite	46	Ferrihydrite	19	Lepidocrocite	11	FeIII citrate	24	100
Arp2 mFSi	0.0130281	Chlorite	46	Ferrihydrite	15	Lepidocrocite	14	FeIII citrate	26	100
Arp2 Cl	0.0395401	Chlorite	25	Ferrihydrite	20	Lepidocrocite	14	FeIII citrate	41	100
Arp2 mCl	0.0545088	Chlorite	23	Ferrihydrite	21	Lepidocrocite	15	FeIII citrate	42	100
Arpd FSa	0.1353997	Chlorite	44	Magnetite	11	Ferrihydrite	35	FeIII citrate	10	100
Arpd CSi	0.0491993	Chlorite	41	Ferrihydrite	23	Lepidocrocite	19	FeIII citrate	18	100
Arpd mCSi	0.0141161	Chlorite	41	Ferrihydrite	21	Lepidocrocite	18	FeIII citrate	21	100
Arpd FSi	0.0246098	Chlorite	36	Ferrihydrite	21	Lepidocrocite	16	FeIII citrate	27	100
Arpd mFSi	0.0442138	Chlorite	41	Ferrihydrite	13	Lepidocrocite	16	FeIII citrate	31	100
Arpd Cl	0.035265	Chlorite	18	Ferrihydrite	26	Lepidocrocite	18	FeIII citrate	38	100
Arpd mCl	0.0274329	Chlorite	17	Ferrihydrite	28	Lepidocrocite	20	FeIII citrate	35	100
Brd1 FSa	0.0858789	Chlorite	49	Nontronite	27	Hematite	13	Magnetite	11	100
Brd1 CSi	0.0526621	Chlorite	35	Ferrihydrite	29	Lepidocrocite	16	FeIII citrate	20	100
Brd1 mCSi	0.0123727	Chlorite	31	Ferrihydrite	31	Lepidocrocite	16	FeIII citrate	22	100
Brd1 FSi	0.2231373	Chlorite	66	Goethite	21	Lepidocrocite		FeIII citrate	13	100
Brd1 mFSi	0.011673	Chlorite	27	Ferrihydrite	30	Lepidocrocite	13	FeIII citrate	30	100

Brd1 Cl	0.0242448	Chlorite	10	Ferrihydrite	40	Lepidocrocite	19	FeIII citrate	31	100
Brd1 mCl	0.0230121	Chlorite	9	Ferrihydrite	41	Lepidocrocite	19	FeIII citrate	31	100
Brd2 FSa	0.0843658	Chlorite	51	Nontronite	31	Hematite	10	Magnetite	8	100
Brd2 CSi	0.0699578	Chlorite	36	Ferrihydrite	24	Lepidocrocite	12	Fe III citrate	29	100
Brd2 mCSi	0.0539459	Chlorite	47	Ferrihydrite	24	Lepidocrocite	14	Lepidocrocite	15	100
Brd2 FSi	0.0467505	Chlorite	29	Ferrihydrite	24	Lepidocrocite	11	Fe III citrate	36	100
Brd2 mFSi	0.0382681	Chlorite	36	Ferrihydrite	23	Lepidocrocite	11	Fe III citrate	30	100
Brd2 Cl	0.1897291	Chlorite	41	Goethite	22	Magnetite	15	FeIII citrate	22	100
Brd2 mCl	0.0416766	Chlorite	11	Ferrihydrite	40	Magnetite	6	Fe III citrate	43	100